Atlantic $\delta^{13}C$ Deep-water Seesaw Controlled by Antarctic Sea Ice Over the Last 800 ka

João M. Ballalai[1, 2]*, Natalia Vázquez Riveiros[2], Thiago P. Santos[3], Rodrigo A. Nascimento[3], Manfred Mudelsee[4,5,6], Patrícia Piacsek[7], Igor M. Venancio[1], Bruna B. Dias[8], André Belem[9], Karen B. Costa[10], Felipe Toledo[10], Ana Luiza S. Albuquerque[3]

[1] Geochemistry Department, Fluminense Federal University, Niterói, Brazil

[2] UMR 6538 Geo-Ocean, CNRS, IFREMER, UBO, UBS, Plouzané, France

[3] Programa de Pós-Graduação Dinâmica dos Oceanos e da Terra (DOT-UFF), Fluminense Federal University

[4] University of Potsdam, Institute of Geosciences, Potsdam, Germany

[5] Climate Risk Analysis, Kreuzstrasse 27, Heckenbeck, 37581Bad Gandersheim, Germany

[6] Alfred Wegener Institute, Helmholtz Centre for Polar and Marine Research, Bussestrasse 24, 27570 Bremerhaven, Germany

[7] Centro de Geociencias, Universidad Nacional Autónoma de México (UNAM), Campus UNAM Juriquilla, Querértaro, Qro, Mexico, 76230

[8] School of Arts, Sciences and Humanities, University of São Paulo, São Paulo, Brazil

[9] Oceanographic Observatory, Fluminense Federal University, Niterói, Brazil

[10] South Atlantic Paleoceanography Laboratory, Oceanographic Institute, University of Sao Paulo, Sao Paulo, Brazil

Corresponding author: João M. Ballalai (joaoballalai@id.uff.br)

Full postal address: Chemistry Institute – Geochemistry Department, 5th floor. Outeiro São João Baptista s/n - Centro - Niterói, RJ - Brazil

Abstract

Over the last 800 ka, significant climatic events such as the Mid-Brunhes Transition (MBT, 430 ka) have profoundly impacted Earth's climate system. The Atlantic Meridional Overturning Circulation (AMOC) and deep-water formation rates around Antarctica have been invoked as vital factors in these climatic events. The MBT marks an increase in the intensity and frequency of glacial-interglacial (G-IG) cycles. Long-term changes in deep-water variability may have played a critical role in providing positive feedback that amplified orbital effects on climate by regulating the ventilation of CO_2 in the Southern Ocean through

`

atmospheric and oceanic connections. This study presents a new 770 ka benthic foraminifera $\delta^{13}C$ record from sediment core GL-854 retrieved from the western South Atlantic at 2200 m water depth. We compared this record to published $\delta^{13}C$ data from the eastern South Atlantic to investigate the zonal $\delta^{13}C$ gradient variability ($\Delta\delta^{13}C_{w-e}$) of North Atlantic Deep Water (NADW). Our results reveal that $\Delta\delta^{13}C_{w-e}$ G-IG variability responds to a "deep-water seesaw" driven by increased influence of Antarctic Bottom Water (AABW) at mid-depths promoted by a shallower AMOC during intense glacial stages. RAMPFIT analysis of the $\Delta\delta^{13}C_{w-e}$ record shows an oscillation between four AMOC modes controlled by orbitally-triggered variations in Antarctic sea ice extent, which promoted NADW intensification in particular after 300 ka. Spectral power in the obliquity and eccentricity domains identified in our record suggests that the orbital forcing on Antarctic sea ice extent is propagated toward subtropical regions through controls over the deep-water seesaw. Our interpretation proposes a framework connecting sea-ice and ocean-atmosphere dynamics to deep-water geometry within the South Atlantic basin, which ultimately contributed to the climate changes during the Late Pleistocene.

Keywords: Deep-water mass geometry; Deep-water seesaw; $\delta^{13}C$ variability; Atlantic Meridional Overturning Circulation; North Atlantic Deep Water intensification; long-term climate changes; Mid-Brunhes Transition

1. Introduction

Through the last ca. 800 ka, periodic ~ 100 ka oscillations of the climate system named glacial-interglacial (G-IG) cycles have been imprinted on paleoclimate records, such as those of oxygen isotope ratios of benthic foraminifera reflecting the variability of global ice volume (Imbrie et al., 1993; Lisiecki and Raymo, 2005). It is commonly assumed that the pacing of these cycles is controlled by summer insolation forcing at high latitudes of the Northern Hemisphere (Hays et al., 1976) and that mechanisms controlling atmospheric carbon dioxide play a vital role in modulating the amplitude of G-IG cycles. Ice core records reveal that atmospheric CO_2 has varied between 180 and 280 ppm following a G-IG variability (Petit et al., 1999; Siegenthaler et al., 2005; Lüthi et al., 2008). Several distinct mechanisms have been proposed to explain the observed 100 ppm glacial atmospheric CO_2 drawdown, mainly connected to glacial carbon storage in the deep ocean and a corresponding reduction of ocean-atmosphere fluxes in the Southern Ocean (Sigman and Boyle, 2000; Yu et al., 2016).

The Atlantic Meridional Overturning Circulation (AMOC) has undergone significant long-term trends characterized by periods of stability and instability, fluctuations in strength and geometry. On G-IG time scales, changes in deep-water distribution alter the large-scale patterns of the carbon cycle by regulating global atmospheric CO_2 (Sigman and Boyle, 2000; Toggweiler, 1999; Toggweiler et al., 2006). During the last glacial period, fresher and less dense surface waters would have reduced the formation and the extension of the glacial version of North Atlantic Deep Water (NADW), the Glacial North Atlantic Deep/Intermediate Water (GNAIW) (Curry and Oppo, 2005). Reduced production in NADW during glacial periods may have been balanced by increased Antarctic Bottom Water (AABW) formation driven by stronger winds and enhanced sea-ice formation, establishing a deep-water seesaw between NADW/GNAIW and AABW (Broecker, 1998; Buizert and Schmittner, 2015).

Water mass geometry and mixing across the Atlantic basin during different states of the AMOC have been investigated using the $\delta^{13}C$ proxy (Curry and Oppo, 2005; Duplessy et al., 1988; Lund et al., 2015; Peterson and Lisiecki, 2018; Schmiedl and Mackensen, 1997; Voigt et al., 2017). Benthic foraminifera $\delta^{13}C$ measurements on *Cibicidoides wuellerstorfi* species are considered to record deep-water dissolved inorganic carbon isotopic values ($\delta^{13}C_{DIC}$) (Duplessy et al., 1988; Lea, 1995; Oppo and Horowitz, 2000). The oceanic vertical $\delta^{13}C_{DIC}$ profile mirrors upper ocean biological productivity. During photosynthesis, ^{12}C from surface waters is preferentially uptaked leaving surrounding waters ^{13}C-enriched, while remineralization leaves the deep ocean ^{13}C-depleted. However, other factors can influence $\delta^{13}C_{DIC}$, including nutrient distribution, CO_2 air-sea exchanges during water mass formation, end-member changes, and, particularly, the redistribution of seawater $\delta^{13}C$ by ocean circulation.

AMOC intensity is coupled to the NADW formation rate (Rahmstorf, 2006), which is connected to the Southern Hemisphere climate via NADW upwelling in the Southern Ocean (Marshall and Speer, 2012; Talley, 2013). Variations in the upwelling rate around Antarctica would, in turn, affect deep-water convection in the North Atlantic by regulating the return flow of circulation. Reduced NADW formation enhances the formation and expansion of nutrient- and respired carbon-enriched AABW, which is believed to have helped to reduce atmospheric CO_2 critically due to increased deep-water stratification and diminished ocean-atmosphere exchange that reduced CO_2 outgassing from the Southern

`

Ocean (Stephens and Keeling, 2000; Ferrari et al., 2014; Nadeau et al., 2019). Therefore, modifications in the balance between NADW and AABW (i.e., the "deep-water seesaw") are critical for long-term climate changes, playing an important role in climatic transition such as the Mid-Brunhes Transition (MBT; Jansen et al., 1986; Yin, 2013; Barth et al., 2018).

The MBT marks the shift between two different climatic states defined by an increasing amplitude of G-IG cycles; orbital parameters are also thought to play a key role in this transition (Jansen et al., 1986; Yin and Berger, 2010; Yin, 2013). During the more recent Marine Isotope Stages (MIS) (430-0 ka), both Antarctic temperatures and atmospheric CO_2 concentrations were significantly higher than before in the previous "lukewarm interglacials" (800-430 ka) (Jouzel et al., 2007; Lüthi et al., 2008).

Long-term AMOC variations might have played a critical role in providing positive feedbacks that magnify the orbital effects on climate (Barth et al., 2018; Holden et al., 2011; Kemp et al., 2010). Understanding these mechanisms is essential for deciphering the climate response to both external and internal forcings. In particular, reconstructions of the South Atlantic Deep Western Boundary Current (DWBC) variability and geometry, a critical component of AMOC for inter-hemispheric heat fluxes exchange, are needed to understand how transitions between distinct modes of circulation affected the carbon cycle during the Late Pleistocene. The water mass dynamics at mid-depths (i.e., 2000 – 2500 m) are particularly interesting since they mark the boundary between northern- and southern-sourced deep-water masses (Curry and Oppo, 2005; Muglia and Schmittner, 2021). However, their accurate evaluation has been hampered by the lack of continuous long-term records in the western South Atlantic (WSA).

Here, we present a new 770 ka $\delta^{13}C$ record based on the benthic foraminifera species *Cibicidoides wuellerstorfi* from sediment core GL-854 retrieved from the WSA (25°12′S, 42°37′W) at 2200 m water depth (Fig. 1). We compare our record with published $\delta^{13}C$ data from the Deep Eastern Boundary Current (DEBC) to investigate the zonal $\delta^{13}C$ gradient variability ($\Delta\delta^{13}C_{w-e} = \delta^{13}C_{GL-854} - \delta^{13}C_{ODP\ 1264}$) of NADW over the last ca. 800 ka. Our $\Delta\delta^{13}C_{w-e}$ record reveals oscillations between distinct modes of AMOC controlled by the orbitally-triggered Antarctic sea-ice variability. We establish the connection between long-

`

term trends in AMOC, sea ice, and orbital forcing over the Late Pleistocene, elucidating the role of AMOC on the climate transition across the MBT.

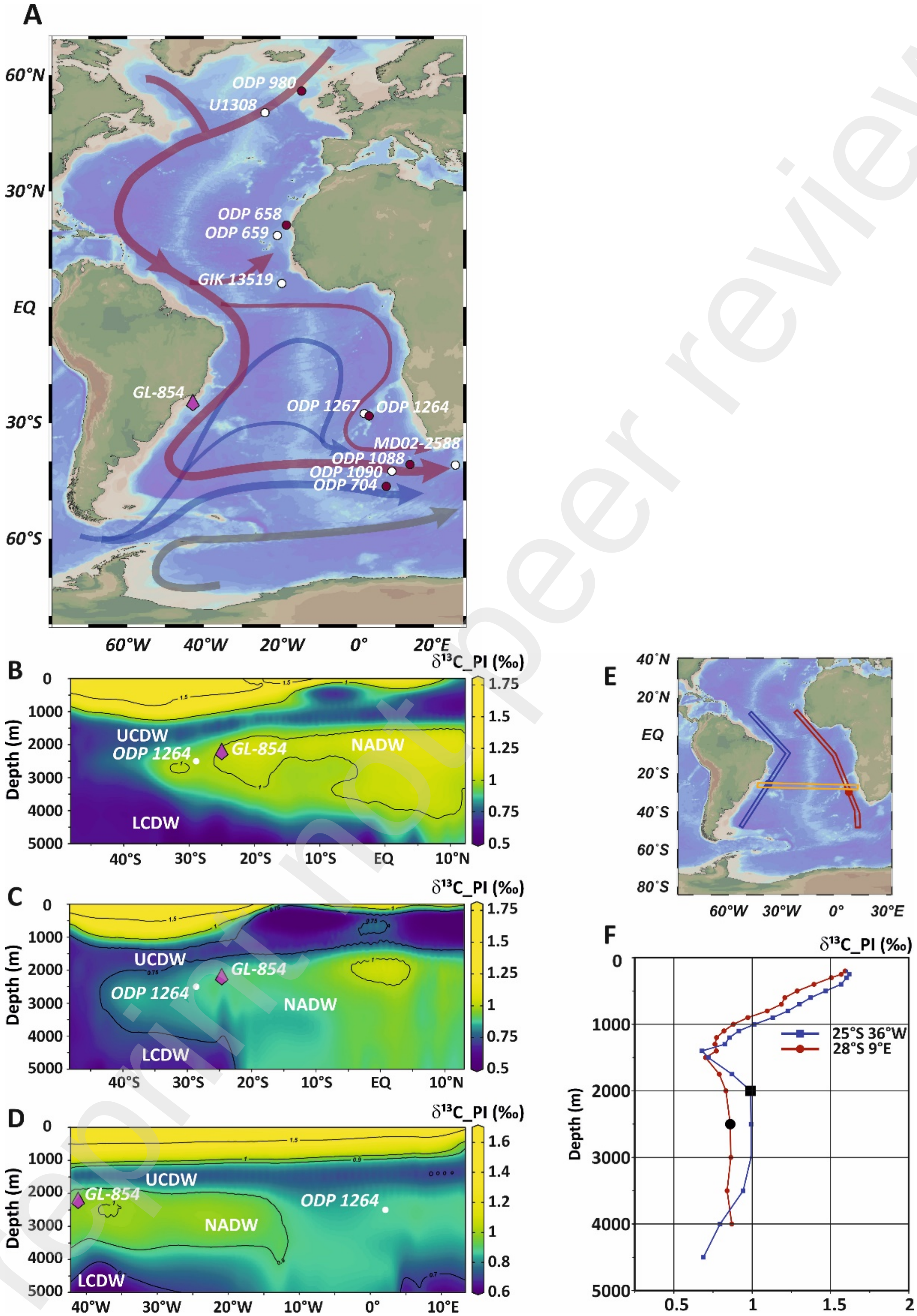

Figure 1 – A) Position of core GL-854 (red pin, this study) in the western South Atlantic (WSA) and other marine records discussed in this work (red circles: mid-depth core site, white circles: deep core sites): North Atlantic sites: ODP Site 980 (Flower et al., 2000), IODP Site U1308 (Hodell and Channell, 2016), ODP Sites 658, 659 (Sarnthein and Tiedemann, 1989), GIK 13519 (Sarntheim et al., 1984); South Atlantic sites: ODP Sites 1264, 1267 (Bell et al., 2014), and 704 (Hodell, 1993), MD02-2588 (Starr et al., 2021), ODP Sites 1088 and 1090 (Hodell et al., 2003). B) to F) sections showing pre-industrial $\delta^{13}C$ distribution in the water column (Eide et al., 2017). E) Meridional sections of the B) western and C) eastern South Atlantic encompassing the subtropical South Atlantic sites; D) subtropical South Atlantic zonal section. Sections are represented in the map by the blue, red, and yellow colors, respectively. F) Preindustrial vertical $\delta^{13}C$ profiles of the closest stations to GL-854 (blue) and to ODP Site 1264 (red) (Eide et al., 2017). The black square and circle are the closest data points to the depth of the cores. The figure was produced using Ocean Data View (Schlitzer, 2021).

2. Material and Methods

2.1 Sediment cores

We conducted an analysis of marine sediment core GL-854, collected by Petrobras (Rio de Janeiro, Brazil) in the subtropical western South Atlantic (25°12′S, 42°37′W, 2220 m water depth, 20.38 m long; Fig. 1) during the Fugro Explorer Campaign in 2007. Ten cm^3 of sediment were collected at 5 cm intervals through the entire core and disaggregated by soaking in distilled water in an orbital shaker. Samples were washed over a 63 µm mesh sieve, oven-dried for 24 h at 60 °C, and stored in acrylic flasks.

Our main interpretations are based on direct comparison to records from the sediment core at ODP Site 1264 (28°31.95′S, 2°50.73′W, 2505 m water depth and 283 m long; Zachos et al., 2004), retrieved at similar water depth in the Walvis Ridge, on the subtropical eastern South Atlantic, to calculate zonal $\delta^{13}C$ gradient (i.e., $\Delta\delta^{13}C_{w\text{-}e}$, Fig. 2B).

2.2 Study area

Core GL-854 site is located off the Brazilian coast at the Santos Basin continental slope (SE Brazilian margin) in the subtropical WSA (Fig. 1). The uppermost (0–600 m) wind-driven circulation at this site is dominated by the southward-flowing Brazil Current (BC), which is the surface WBC of the South Atlantic Subtropical Gyre (Stramma and England, 1999). The site of GL-854 presents punctually seasonal vertical carbon export to the bottom in some periods throughout the core, but the phytodetritus effect does not significantly affect benthic $\delta^{13}C$ (de Almeida et al., 2015; Mackensen et al., 1993). This region is a low-latitude oligotrophic area without large river influence, so the supply of terrigenous sediments to the slope is limited, implicating that ocean currents are probably the primary driver for the sedimentary dynamics at the core site (Razik et al., 2015).

In contrast, the subtropical eastern South Atlantic hosts one of the most intense upwelling zones in the world, the Benguela Upwelling System (BUS). At present, the northern BUS presents relatively higher productivity at the surface layers only near the coast (Siegfried et al., 2019). The lower rate of nutrient flux to the euphotic zone farther offshore promotes considerably reduced surface primary productivity and lower vertical transport of carbon to the sea floor, reducing the impact on carbon benthic $\delta^{13}C$ (Bordbar et al., 2021; Mackensen et al., 1993). ODP Site 1264 was drilled in Walvis Ridge, chosen during Leg 208 as a promising site to record global ocean carbon chemistry and circulation changes without significant BUS influences (Zachos et al., 2004).

The modern ocean circulation structure of the western and eastern sectors of the South Atlantic have quite similar deep water masses distributions (Fig. 1). At present, high $\delta^{13}C$ NADW is present between 1200 and 4000 m, and lower $\delta^{13}C$ AABW occupies abyssal depths below 4000 m (Stramma and England, 1999). At higher southern latitudes, NADW splits CDW into two parts: an upper (UCDW) and a lower (LCDW) branch (Piola and Matano, 2019; Stramma and England, 1999). During the last glacial period, high $\delta^{13}C$ values (~1.5 ‰) were centered at 1500 m, corresponding to the well-ventilated and shallower GNAIW (Curry and Oppo, 2005; Duplessy et al., 1988; Lynch-Stieglitz et al., 2007). Below (i.e., at depths > 2000 m), a pool of "old" and isotopically light carbon was present due to increased deep-water isolation and the accumulation of respired carbon (Curry and Oppo, 2005; Schmittner and Lund, 2015; Skinner et al., 2010). The commonly termed Southern Component Water (SCW) has low $\delta^{13}C$ (~ -0.9 ‰) and occupies deeper South Atlantic layers because of intensified export of AABW from the Southern Ocean (Curry and Oppo, 2005). Focusing on the western South Atlantic sector, (Curry and Oppo, 2005) suggest that GNAIW penetrated southward as far as 30°S latitude, while deeper SCW may have penetrated as far north as 60°N. These findings are consistent with previous nutrient reconstructions at 28°S,

`

showing that a relative nutrient-depleted water mass was present during the LGM at 1500 m, above expanded, more nutrient-rich SCW (Oppo and Horowitz, 2000).

The glacial shallowing of this boundary between NADW and AABW might correspond to the vertical chemocline at depths of 2000 - 2500 m, a persistent feature of glacial water mass architecture in the Atlantic sector of the Southern Ocean during Pleistocene glacial periods (Hodell et al., 2003) that can also be seen on the Southeastern Atlantic (Marchitto and Broecker, 2006).

2.3 Stable isotopic carbon composition

In this work, we present a new benthic $\delta^{13}C$ record combined with the published benthic oxygen isotope ($\delta^{18}O$) (de Almeida et al., 2015) of piston core GL-854 (Fig. 2C and D). At least three shells of the epibenthic foraminifera *Cibicidoides wuellerstorfi* (> 150 μm) were handpicked using a binocular microscope and analyzed at the *Universitat Autonoma de Barcelona*, Spain, on a Finnigan MAT252 mass spectrometer with an automated carbonate device. Results are presented in parts per thousand versus the Vienna Pee Dee Belemnite (VPDB) scale. The $\delta^{13}C$ record of ODP Site 1264 is also based on *C. wuellerstorfi* (Bell et al., 2014), which avoids biases due to distinct vital effects of different species.

2.4 GL-854 age model

The age model of the GL-854 core was obtained through a combination of three calibrated AMS 14C ages (de Almeida et al., 2015) and the visual alignment of our benthic $\delta^{18}O$ record to the global LR04 $\delta^{18}O$ stack (Lisiecki and Raymo, 2005) following the recommendations of Blaauw et al. (2018) and Lacourse and Gajewski (2020). Radiocarbon dating were measured on *Globigerinoides ruber* (white) shells at the National Ocean Science Accelerator Mass Spectrometer Facility (NOSAMS) at Woods Hole Oceanographic Institution (WHOI). The radiocarbon ages calibration is detailed in de Almeida et al. (2015). The benthic $\delta^{18}O$ alignment was performed with the software AnalySeries (Paillard et al., 1996). The age model allowed the estimation of a mean sedimentation rate of 4.3 cm/ka throughout the core, which therefore covers the period between ca. 4 and 772 ky (Supplementary Fig. 1).

The age model for ODP Sie 1264 is based on the *Cibicidoides* spp. $\delta^{18}O$ records are primarily used to map the mcd scale of Site 1267 onto Site 1264 to combine data to form a single continuous record based on the Site 1264 depth scale (Walvis Stack). The Walvis Stack $\delta^{18}O$ and Site 1264 were stratigraphically aligned to the LR04 benthic stack (Lisiecki and Raymo, 2005). Age controls from calcareous nannofossil and paleomagnetic reversal were used, producing an excellent general agreement with the $\delta^{18}O$-derived age model. The original benthic isotopic data have a mean temporal resolution of approximately 5.15 kyr (Bell et al., 2014). More details about ODP Site 1264 age model can be found in Bell et al. (2014).

2.5 RAMPFIT and spectral analysis

Quantitative time-series analyses are critical to support interpretations of long-term time-series data statistically. RAMPFIT is a statistical software valuable for quantifying and describing past climate transitions accurately in paleoclimatic records that are usually done visually (Mudelsee, 2000). It is based on the weighted least-squares method, and produces a ramp fitting to the record by estimating levels before and after a transition assuming a linear change between two change points in time and delivering a measure of their uncertainties (1 s.d.) based on bootstrap simulations. Each of the 10000 moving block bootstrap simulations (Mudelsee, 2014) uses randomly selected blocks of ramp regression residuals and assures robustness against (1) the presence of non-normal distributions and (2) the existence of serial dependence; both are typical paleoclimatic features that "plague" conventional climate time series analysis. This technique provides one ramp by each performed analysis giving two change points that occurred from a constant level before towards new constant values (i.e., in the y-axis) after the transition. However, oceanographic and climatic records do not necessarily follow this simplistic pattern and might contain multiple transitions, in which level changes across change points are out of the uncertainties and thus statistically relevant (Röthlisberger et al., 2008). Therefore, the subjective selection of the search window for the fit interval is relevant and might influence the result. Mean Knn-smoothing is a non-parametric trend estimation that calculates the mean over the k nearest neighbors by shifting a window across the time axis. Analyzing the knn-smoothed trend in our $\Delta\delta^{13}C_{w-e}$ record allows a first estimation of its general variability, providing a starting point to determine periods for brute-force inspection and search of transitions and ultimately define possible statistically-based change point locations.

We performed RAMPFIT analysis three times in our $\Delta\delta^{13}C_{w-e}$ record, applying a full search range each time over three subsections. It revealed a younger transition from the search range between 2.3 to 458 ka, a transition interval from the search range between 257 to 640 ka, and an older transition from the search range between 464 to 771 ka. These three ramps and six change points best fit the trends observed in our record, which can therefore be subdivided into four different phases (Fig. 2A). Changing the selected boundaries of the transition intervals did not lead to significantly altered change-point estimation results, confirming the robustness of the change-point regression model.

REDFIT spectral analysis (Schulz and Mudelsee, 2002) was performed to identify statistically significant periodicities on the GL-854 $\delta^{13}C$ and $\Delta\delta^{13}C_{w-e}$, Dome C Atarctic ice core sea-salt Na (ssNa; (Wolff et al., 2006) and core MD08-2588 IRD count (Starr et al., 2021) records (Fig. 3). We used the software PAST v4.03 (Hammer et al., 2001). Setting different segment values for the analysis did not alter the significance of the main frequencies, suggesting robust spectral power (Fig. 4).

3 Results

3.1 *Benthic $\delta^{13}C$ and zonal $\delta^{13}C$ gradient evolution*

Our $\delta^{13}C$ record ranges from -0.33 ‰ to 1.49 ‰, with the most depleted isotopic composition at ca. 263 ka (MIS 8) and most enriched at ca. 499 ka (MIS 13) (Fig. 2C). The average value is 0.7 ‰. The $\delta^{13}C$ value at the top of the core is 1.1 ‰, in good agreement with the modern NADW $\delta^{13}C$ end-member value (Kroopnick, 1985). The largest variation present in our record corresponds to the enrichment of ~ 1.4 ‰ during the MIS 8/7 transition. Similarly, the end of the MIS 9 toward glacial minima during MIS 8 displays a drastic reduction in the $\delta^{13}C$ values from 1.1 ‰ to -0.33 ‰, also shifting by ~ 1.4 ‰. The $\delta^{13}C$ transitions during glacial Terminations are more abrupt and have higher amplitude after the MBT than before. The isotopic shift through Termination V (MIS 12/11, ~ 1.0 ‰) marks the transition toward the first intense interglacial after the MBT and corresponds to the first abrupt G-IG $\delta^{13}C$ shift. However, the $\delta^{13}C$ differences between glacial minima and interglacial maxima are generally higher before the MBT.

`

The benthic zonal $\delta^{13}C$ gradient between both sides of the South Atlantic basin was calculated by (1) interpolating the highly resolved series (GL-854; Fig. 2C) to the time scale of the more coarsely resolved series (ODP Site 1264; Fig. 2C) and then by (2) subtracting the isotopic values of the interpolated GL-854 record from the ODP 1264 series, that is, $\Delta\delta^{13}C_{w-e} = \delta^{13}C_{GL-854} - \delta^{13}C_{ODP\ 1264}$ (Fig. 2A).

The $\Delta\delta^{13}C_{w-e}$ (Fig. 2A) record ranges from -0.66 ‰ to 0.84 ‰, with the lowest isotopic gradient at ca. 300 ka (MIS 8) and the highest at ca. 252 ka (MIS 7). The average of the $\Delta\delta^{13}C_{w-e}$ record is 0.16 ‰. G-IG variability is well marked in the record; minimum $\Delta\delta^{13}C_{w-e}$ values (i.e., reduced western-eastern $\delta^{13}C$ gradient) seem to be a persistent feature when fully cold glacial conditions are established. Through most of the $\Delta\delta^{13}C_{w-e}$ record, the gradient is higher during interglacial periods, with an amplitude closely matching the modern gradient of 0.13 ‰ between these sites. The gradient between both margins is inverted during cold glacial stages (e.g., MIS 12 and MIS 8), driven by ^{13}C-depleted excursions in the GL-854 $\delta^{13}C$ record. RAMPFIT-calculated change points identify the transitions that separate the long-term $\Delta\delta^{13}C_{w-e}$ variability into four main phases: (I) ca. 800-630 ka, with low $\Delta\delta^{13}C_{w-e}$ average values of 0.01 ± 0.06 ‰; (II) ca. 630-465 ka, with intermediate values of 0.23 ± 0.054 ‰, (III) ca. 460-300 ka, with low $\Delta\delta^{13}C_{w-e}$ values of 0.00 ± 0.08 ‰; (IV) ca. 300 ka to 4.4 ka, with the highest level of 0.31 ± 0.06 ‰.

4 Discussion

4.1 *Atlantic deep-water seesaw: long-term trends in AMOC strength*

Past variations in AMOC strength would have substantially affected sites between 1000 and 2500 m water depth, increasing the $\delta^{13}C$ values due to pronounced southward penetration of isotopically heavier NADW (Muglia and Schmittner, 2021). In order to verify if the site of core GL-854 does register variations on NADW, we have compared its benthic $\delta^{13}C$ record to that of ODP Site 980, at 2180 m water depth and 55°N, in the vicinity of the production sites, and commonly used to represent the end-member value of mid-depth NADW (Flower et al., 2000). The GL-854 $\delta^{13}C$ record shows similar downcore variability and absolute values to ODP Site 980, including similar Holocene $\delta^{13}C$ values (Fig. 2C).

`

Punctual discrepancies (i.e., lower isotopic values during MIS 5 off Brazil) are likely related to differences in temporal resolution between the records and to short-lived local effects. This suggests that the NADW signal has been carried to the Brazilian site throughout the last ca. 800 ka and allows us to assume that our $\delta^{13}C$ record represents NADW variability in the South Atlantic.

To investigate the NADW zonal distribution within the South Atlantic, we look at the zonal $\delta^{13}C$ gradient between the DWBC and DEBC (i.e., $\Delta\delta^{13}C_{w-e}$, Fig. 2A) calculated from the GL-854 $\delta^{13}C$ record minus that of ODP Site 1264 (Fig. 2C). The DWBC in the WSA bifurcates twice, once near the equator and afterward at 22 °S, forming NADW eastward zonal flows (Stramma and England, 1999). In present-day conditions, the DWBD presents a slightly ^{13}C-enriched NADW signal than at the eastern margin, characteristic of more ventilated waters (Fig. 1B and C). Also, there is no vertical change in the $\delta^{13}C$ profiles from both sides of the basin between 2000 and 3000 m water depth (Fig. 1F), which implies that the 300-m depth difference between the two cores is inferred to be irrelevant to explain the discrepancies between the records, in particular during interglacial periods. Therefore, positive values in $\Delta\delta^{13}C_{w-e}$ during interglacial periods must represent an enhanced influence of better-ventilated waters of higher NADW $\delta^{13}C$ on the WSA. Hence, instabilities in our $\Delta\delta^{13}C_{w-e}$ record are assumed to result from changes in the zonal $\delta^{13}C$ distributions within the same water mass between both margins of the South Atlantic.

The $\Delta\delta^{13}C_{w-e}$ record shows a drastically reduced gradient consistently during glacial stages, to the point that it is reversed during fully glacial conditions throughout most of the record (e.g., MIS 4, MIS 8, MIS 10, MIS 12, MIS 16, and MIS 18), except during MIS 6 and MIS 14 (Fig. 2B). This pattern likely responds to a configuration of reduced ocean circulation state during glacial periods, with less well-ventilated waters reaching both sites, decreasing the $\Delta\delta^{13}C_{w-e}$ record. Although the first negative excursion in the record appears during the glacial stage MIS 16, this glacial dynamic becomes more marked and regular from the super-glacial stage MIS 12. The low $\Delta\delta^{13}C_{w-e}$ values during MIS 16 may represent the early deep-water response to the first manifestation of the 100-ky cycle pacing of G-IG transitions (Hays et al., 1976; Imbrie et al., 1993; Mudelsee and Schulz, 1997; Diekmann and Kuhn, 2002), which reached its full strength after MIS 12 (Berger and Wefer, 2003). The decrease in

NADW production expected during extremely cold climates such as MIS 12 might have promoted a particularly marked AMOC slowdown (Droxler et al., 2003; Vázquez Riveiros et al., 2013), which promoted a shallower boundary between NCW and SCW and increased the SCW influence up to ~ 2200 m depths. A similar pattern is present in the following glacial periods, MIS 10 and MIS 8.

Therefore, we interpret our $\Delta\delta^{13}C_{w-e}$ G-IG variability as a deep-water response sensitive to depth variability of the interface between the shallow and deep cells of the AMOC related to different oceanic circulation states. However, since $\Delta\delta^{13}C_{w-e}$ is based on a gradient, dependent on the resolution, interpolation methods, and age model construction of each $\delta^{13}C$ record, care must be taken to avoid over-interpretation of the signals.

RAMPFIT results reveal longer-term trends in the $\Delta\delta^{13}C_{w-e}$ record beyond G-IG variability. Six change points subdivided our record into four distinct statistically significant phases (Fig. 3A); the transitions between them are out of the error bars, attesting to the high sensibility of our record to east-west asymmetry in the deep ocean ventilation. Relatively higher $\Delta\delta^{13}C_{w-e}$ values respond to a more pronounced ^{13}C-enriched NADW signal delivered to the WSA rather than to the eastern margin. Therefore, we interpret the gradient increase after ca. 300 ka (phase IV, with the highest gradient values) as NADW intensification probably associated with the onset of vigorous AMOC after the MBT (Caley et al., 2012).

The latitudinal gradient based on the $\delta^{13}C_{DIC}$ of stack representative of northern and southern component waters (Barth et al., 2018) composed of several marine cores decreases around 500 ka (Fig. 2B). A low latitudinal gradient implies enhanced southward penetration of NADW, while high values indicate enhanced northward penetration of AABW (Barth et al., 2018). The RAMPFIT analysis reveals a change point on this record at the end of MIS 13, which agrees with a change point on the $\Delta\delta^{13}C_{w-e}$ record between phases II and III (Fig. 2A and B). However, the zonal gradient only intensifies after 300 ka, probably because RAMPFIT phase III is driven by very low glacial gradient levels during MIS 12, MIS 10, and MIS 8, as will be discussed below. Benthic foraminifera assemblage data from GL-854 indicate a major deep-water condition change occurred after MIS 8 (de Almeida et al., 2015). Declining abundances of *Bolivina* spp. coincide with an abrupt increase in *Globocassidulina crassa*, suggesting a transition from reduced bottom-water oxygenation towards stronger bottom currents of more oxygenated waters delivered to the site when $\Delta\delta^{13}C_{w-e}$ reaches its maximum absolute value of 0.84 ‰. In addition, the $\delta^{13}C$ gradient between the Atlantic and Pacific oceans, usually interpreted as an indicator of overturning strength, also intensifies after ca. 300 ka (Bard and Rickaby, 2009; Caley et al., 2012). Moreover, our interpretation that the North Atlantic WBC intensified during phase IV is also supported by surface data evidence that indicates increased cross-equatorial energy transport, with more stable WBC after ca. 300 ka (Billups et al., 2020).

The other identified phases can be related to previous studies discussing long-term circulation patterns oscillating between strong and weak states of AMOC throughout the last ca. 1200 ka, roughly across the MPT and the MBT. For example, Raymo et al. (1997) showed a relatively weaker NADW production and AMOC from 900 ka that intensified after MIS 12. Moreover, an increased vertical $\delta^{13}C$ gradient between the intermediate and deep ocean in the North Atlantic has been found during the same interval, which supports the hypothesis that the deep-water cells shoaled and mixed less in a weak circulation state (Hodell and Channell, 2016), with weaker NADW production and the northward expansion of the AABW (Pena and Goldstein, 2014). Although these findings agree with our phase I, phase II would correspond to an identified transitional period of global circulation reorganization after 650 ka (Schmieder et al., 2000) that we associated with a relatively increased influence of better-ventilated NADW on the WSA. Evidence from modeling studies argues that the period corresponding to our phase III marks the transition after MIS 12 toward the post-MBT world with reduced AABW and enhanced NADW formation during interglacial periods associated with changes in Southern Ocean ventilation (Barth et al., 2018; Yin, 2013). However, it is also related to intensified glacial conditions, which would have reduced our trend estimation to its lower value (see next discussion topic). Therefore, the zonal gradient dynamics proposed here are coherent with these findings regarding long-term trends in AMOC intensity over the last 800 ka, in the scope of circulation changes across the MBT (e.g., Schmieder et al., 2000; Caley et al., 2012; Barth et al., 2018).

It is noteworthy that the phases of different AMOC modes in this study show features of the deep ocean circulation from the middle to late Pleistocene in unprecedented detail from the WSA. The interpretation of this gradient contributes to our understanding of the transition

`

between long-term AMOC modes, presenting oscillations of the deep-water seesaw that would explain the different transition timings reported in the literature of important climatic events such as the MBT. Still, a question remains: Which mechanism controlled the ocean dynamics that drove the long-term trends in the deep-water seesaw?

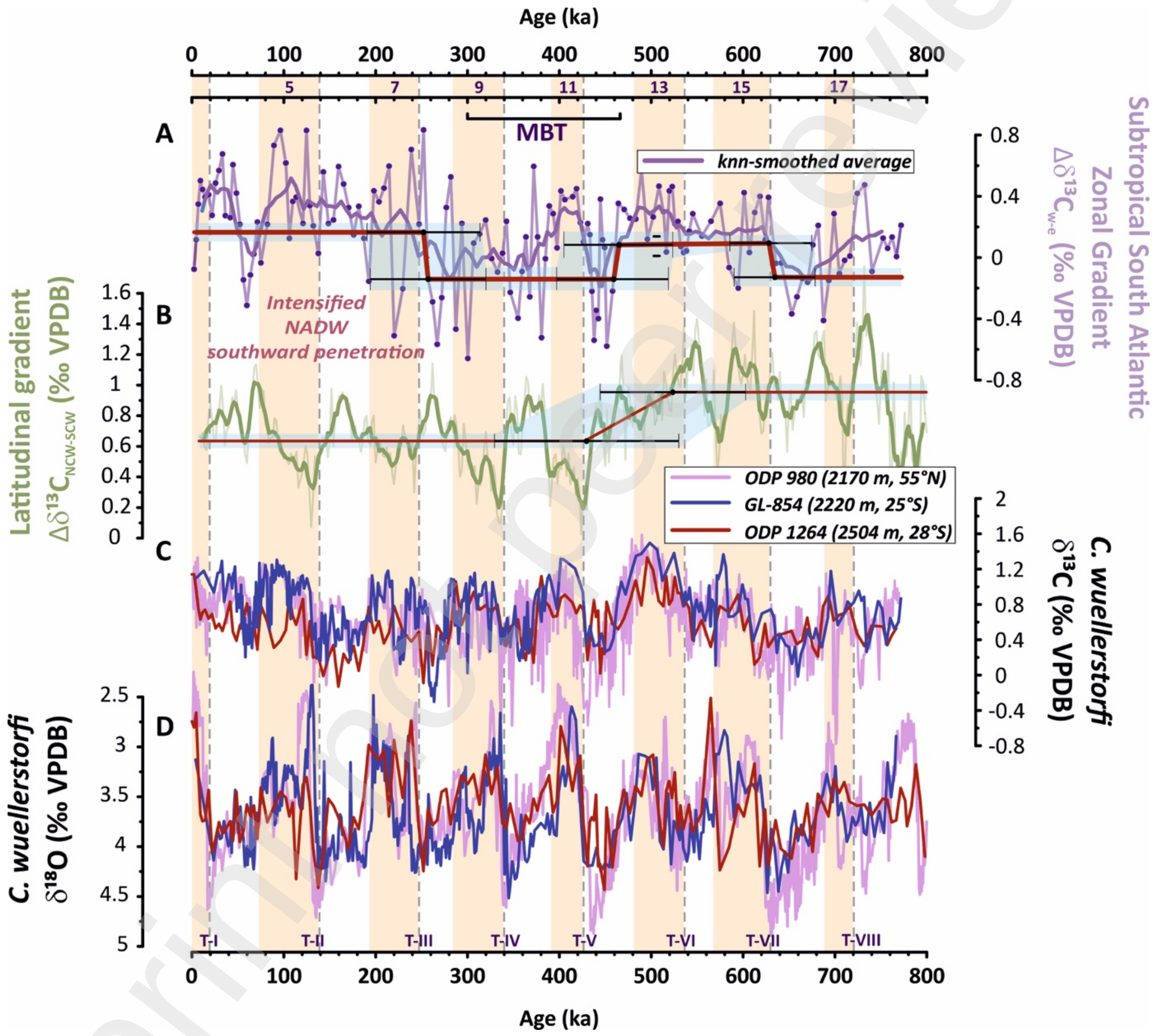

Figure 2 – Long-term RAMPFIT phases revealed in the $\Delta\delta^{13}C_{w-e}$ ($\delta^{13}C_{GL\text{-}854} - \delta^{13}C_{ODP\ 1264}$) record, showing that the subtropical zonal $\delta^{13}C$ gradient between the South Atlantic mid-depth sites increase after the Mid-Brunhes Transition (MBT). A) $\Delta\delta^{13}C_{w-e}$ (light purple line) with eight-point knn-smoothed average (dark purple line); RAMPFIT results (solid red lines) are displayed with their respective uncertainties (light blue shaded area). B) Latitudinal gradient ($\Delta\delta^{13}C_{NCW\text{-}SCW}$, thin light green line) and three-point running average (thick light green line) of the difference between the Northern and Southern Component Water (NCW and SCW, respectively) stacks (Barth et al., 2018).

`

C) $\delta^{13}C$ (‰ VPDB) and D) $\delta^{18}O$ (‰ VPDB) of cores GL-854 (this study; blue), ODP Site 1264 (red) and North Atlantic ODP Site 980 (dark pink). ODP Site 980 represents the end-member of the upper portion of the North Atlantic Deep Water (NADW) in the vicinity of North Atlantic production sites. The comparison between them shows that the NADW signal is carried by the Deep Western Boundary Current (DWBC) to the western South Atlantic. Red bars highlight interglacial periods and dashed lines mark glacial-interglacial transitions over the last ca. 800 ka (Terminations (T) I to VIII are indicated). All records are shown against age (ka).

4.2 Antarctic sea-ice controls on Atlantic deep-water geometry

The Southern Ocean is an essential climate system component as it connects the deep ocean carbon pool with the atmosphere, hosting critical mechanisms acting on G-IG time scales (Sigman and Boyle, 2000; Sigman et al., 2010). Numerical climate model simulations have shown that the expansion of Antarctic sea ice enhanced deep-water stratification during glacial periods, which could have contributed to glacial CO_2 drawdown (Marzocchi and Jansen, 2019). Extended sea ice is thought to have enhanced the formation of denser AABW by intensified salt rejection during sea-ice formation, hindering the mixing with NADW (Paillard and Parrenin, 2004; Bouttes et al., 2010; Jansen and Nadeau, 2016; Jansen, 2017). In addition, the sea ice acted as a lid, reducing air-sea exchange and isolating deep waters (Stephens and Keeling, 2000), thus controlling CO_2 outgassing. The impact of the latitudinal advance of the sea ice on deep-water cells can effectively decouple AABW and NADW, promoting the aging of abyssal water masses due to a drastic reduction in deep-water ventilation that alters the deep-water seesaw (Ferrari et al., 2014; Nadeau et al., 2019). In this context, we consider the Antarctic sea ice as the primary driver controlling the deep-water seesaw in the Atlantic that governs our $\Delta\delta^{13}C_{w-e}$ record, promoting the observed long-term trends in AMOC.

Relatively colder temperatures were registered in the Antarctic EPICA Dome C δD record during the lukewarm interglacials, which may have allowed pronounced sea ice build-up due to reduced interglacial melting (Fig. 3C and d; Jouzel et al., 2007; Wolff et al., 2006). Consequently, the sea-salt-related Na (ssNa) levels, a proxy for Antarctic sea-ice extent, indicate a higher extension during cold G-IG periods before the MBT, leading to a relatively greater volume of AABW formation (Fig. 3C; Ferrari et al., 2014; Barth et al., 2018). Notably, this pattern is particularly evident during RAMPFIT phase I, characterized by a reduced zonal gradient. Furthermore, ssNa glacial levels decrease from enhanced interglacial

`

melting during MIS 15, which results in intermediate G-IG sea ice coverage throughout phase II. Although these changes in sea ice coverage are subtle, they could explain the observed $\Delta\delta^{13}C_{w-e}$ differences between phases I and II. It is worth noting that the transition toward increased NADW influence in the deep Atlantic after the MBT is associated with the change point in the $\Delta\delta^{13}C_{w-e}$ record during MIS 12 and in the meridional gradient (Fig. 2B and C). However, reduced glacial sea ice extent and enhanced interglacial melting can be observed only later at phase IV after ssNa reached the largest extent at the end of phase III (at MIS 8), followed by $\Delta\delta^{13}C_{w-e}$ higher values. Although the relation between ssNa and $\Delta\delta^{13}C_{w-e}$ record can be established and provide insights to explain our RAMPFIT phases, it is difficult fully interpret due to ssNa proxy limitations and perhaps due to the high-frequency variability of the record.

ssNa mostly originated from winter sea ice formation rather than from open ocean waters (Wolff et al., 2003), and therefore, we would expect a coupled response between Antarctic temperatures and sea-ice extension (Fig. 3C and D). However, this relation is reduced under maximum glacial conditions due to a declining proxy response to the increased distance from the source, making sea-salt aerosol concentration decay when carried by wind through higher distances (Röthlisberger et al., 2008, 2010). Thus, the ssNa proxy becomes saturated due to the limited sea salt input when sea ice extent continuously expands and only a small fraction of extra salt reaches the Dome C site. The ssNa aerosol also changes its residence time in response to the hydrological cycle variations, which reduces its fluxes particularly during interglacial periods (Petit and Delmonte, 2009). All these factors limit our interpretation of extreme G-IG values of ssNa, challenging the establishment of an accurate relationship between our zonal gradient and sea ice.

However, the oscillatory behavior of the RAMPFIT phases, particularly phases III and IV, also corresponds well with detrital ice-rafted debris (IRD) particle deposition variability sourced from Antarctica in the Agulhas Plateau region over the studied period (Fig. 3C; Starr et al., 2021). Increased icebergs appearing at this location, far from the source, would demand the expansion of colder atmospheric and sea surface temperatures (SST) and favorable oceanographic conditions for transport and deposition at this latitude (Starr et al., 2021). High IRD counts agree with high ssNa values showing that higher IRD deposition and

`

sea ice are coupled to extreme full glacial conditions (Fig. 3C). There is a remarkable fit between periods of higher IRD and ssNa with periods of negative excursions present in our $\Delta\delta^{13}C_{w-e}$ record. The low $\Delta\delta^{13}C_{w-e}$ phases I (0.01 ± 0.06 ‰) and III (0.00 ± 0.08 ‰) are coeval with periods of relatively larger IRD deposition, which is related to the increased influence of AABW to shallower depths (Fig. 5A and C). Intermediate phase II (0.23 ± 0.054 ‰) is coeval with periods of intermediate levels of IRD, associated with a relatively increasing influence of NADW toward intermediate levels and reduced influence of AABW (Fig. 5B). The enhanced gradient during RAMPFIT phase IV (0.31 ± 0.06 ‰) is coeval with periods of drastic reduction IRD deposition, which decreased AABW formation that promoted the NADW intensification (Fig. 5D).

The persistence of the extremely colder glacial Southern Ocean during MIS 12, MIS 10 and MIS 8 may have increased AABW production, promoting negative excursions in the $\Delta\delta^{13}C_{w-e}$ record that explain the lowest values of phase III (Fig. 5C). Enhanced surface productivity by increased iron deposition in the Southern Ocean during these glacial periods intensified the biological pump (Fig. 3C; Martin, 1990; Martínez-Garcia et al., 2011). It increased vertical transport from the surface to the bottom of ^{13}C-depleted carbon, lowering the AABW $\delta^{13}C$ end member signature. Increased AABW production reduced the mixing with NADW, shallowing the boundary between the AMOC cells to depths close to GL-854 and ODP Site 1264, decreasing the $\Delta\delta^{13}C_{w-e}$ seen in RAMPFIT phase III. A similar scenario may have occurred during MIS 16 and MIS 18, explaining RAMPFIT phase I. We, therefore, assume that enhanced low-$\delta^{13}C$ AABW influence reaching shallower depths promoted a larger decrease in the $\Delta\delta^{13}C_{w-e}$ during intense glacial stages than expected if its variability was exclusively responding to the NADW end member influence.

The influence of buoyancy flux variations in the North Atlantic also needs to be accounted for since it might contribute to increase NADW production (Caley et al., 2014; Weijer et al., 2002). The rate of Indo-Atlantic water exchanges, namely the Agulhas Leakage (AL), contributes to salt build-up in the Atlantic that strengths the AMOC (Beal and Elipot, 2016; Biastoch et al., 2015; Broecker et al., 1990; Gordon, 1986). The salty warm waters from the Indian Ocean enter the South Atlantic through the tip of Africa and are transported by the upper limb of the AMOC toward the North Atlantic, ultimately favoring the formation

`

of NADW (Beal et al., 2011; Caley et al., 2014). The extremely reduced accumulation rate of *G. menardii* in the Southeastern Atlantic is one evidence of the decreased influence of the AL between ca. 800-430 ka (phases I and II; Fig. 3E), which also supports our previous interpretations (Caley et al., 2012). After ca. 430 ka, the AL reactivation is thought to have boosted NADW formation, peaking during glacial Terminations of the last four G-IG cycles (Caley et al., 2012; Peeters et al., 2004). However, the northward advances of the STF during cold MIS 12 and to its lowest latitude of the past 800 ka during MIS 10 (Bard and Rickaby, 2009) might have compensated for the AL contribution to NADW intensification during MIS 11 and MIS 9, which would explain the strong glacial characteristic present in our record during phase III. The AL intensification would explain the differences between RAMPFIT phases I and III (Fig. 5A and C). A diminished Antarctic sea ice surface would regulate both the deep-water seesaw through the decreased formation of AABW (and thus increased NADW volume) and the AL through a more southward position of the STF (and thus increased NADW formation) (Beal et al., 2011; Becquey and Gersonde, 2002; Caley et al., 2014, 2012; Kemp et al., 2010; Martínez-Garcia et al., 2009; Toggweiler et al., 2006).

`

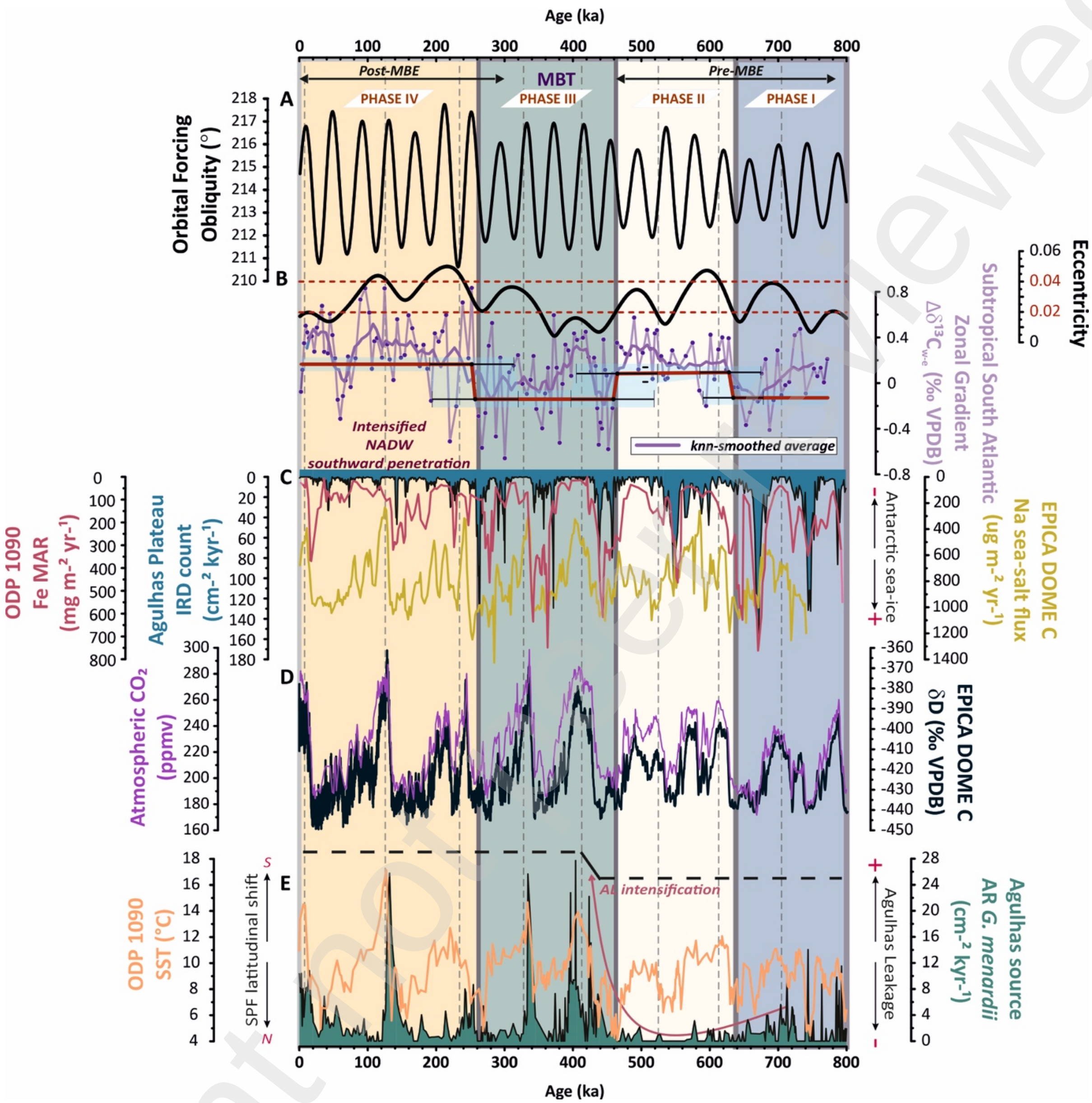

Figure 3 – Evolution of long-term oceanographic and climate records controlling the long-term trend in the deep-water seesaw. A) Obliquity (°; Laskar et al., 2004). B) $\Delta\delta^{13}C_{w-e}$ (light purple line) with 8-point knn-smoothed average (dark purple line); RAMPFIT results (solid red lines) are displayed with respective uncertainties (light blue shaded area). The background blue, light yellow, green, and dark yellow bars indicate RAMPFIT phases I, II, III, and IV, respectively. Black line: eccentricity Laskar et al., 2004). C) Sea-salt Na flux (yellow line; Wolff et al., 2006), Agulhas Plateau Ice-Rafted Debris (IRD) counts (dark blue shaded line; Starr et al., 2021), and ODP Site 1090 Fe MAR (dark pink line; (Martínez-Garcia et al., 2011) records. D) EPICA Dome C δD and atmospheric CO_2 (black and purple lines, respectively; Jouzel et al., 2007; Lüthi et al., 2008). E) ODP Site 1090 sea-surface temperature (SST) (orange line; (Martínez-Garcia et al., 2009) and accumulation rate (AR) of typical Agulhas Leakage fauna (*Glorobotalia mernardii*) from ODP Site 1087 (green filled curve; Caley et al., 2012). Dashed lines represent the glacial-interglacial Terminations. All records are presented against age (ka).

`

4.3 Orbital controls over the Antarctic sea ice

After exploring the mechanism connecting Antarctic sea-ice variability and the transitions between different phases of AMOC intensity, a question follows: which forcing is driving the substantial changes on sea ice capable of promoting these thresholds on circulation? We explore the effects of orbital forcing on promoting a combination of different insolation conditions at southern high-latitudes on the different phase intervals (Supplementary Fig. 3). The REDFIT spectral analyses (Schulz and Mudelsee, 2002) performed on GL-854 $\delta^{13}C$ and $\Delta\delta^{13}C_{w-e}$, Dome C ssNa and Agulhas Plateau IRD records reveal orbital spectral power in the obliquity (~40 ka) and eccentricity (~100 ka) domains with 90% of confidence level (Fig. 4), leading to the assumption that the combined effect of these forcings is influencing the Antarctic sea-ice variability.

Obliquity forcing exerts a predominant role in the high latitudes by controlling the received annual insolation energy, which has a particularly strong effect in the Southern Hemisphere due to the higher thermal capacity of larger ocean areas (Yin and Berger, 2012; Wu et al., 2020). The insolation decreases (increases) under low-obliquity (high-obliquity) periods, decreasing (increasing) ice melting, which likely increases (reduces) the amount of sea ice (Paillard, 2021). This would explain why most negative excursions throughout the $\Delta\delta^{13}C_{w-e}$ record occurred under low obliquity (Fig. 3; Supplementary Figure 3). Mitsui and Boers (2022) discussed the obliquity effects on the climate system over the last 800 ka in the context of the MBT. They propose that the increasing amplitude of obliquity forcing might be responsible for enhancing the amplitude of G-IG cycles after 450 ka. We agree with this hypothesis, but we further suggest that eccentricity might have played an important role in this climate transition by modulating the high-latitude insolation.

Antarctic sea ice dynamics have a strong seasonal character, with a maximum extent during winter months (Wolff et al., 2006). Obliquity drives seasonality, which varies in function of summer insolation at Southern high latitudes, and eccentricity controls the intensity and duration of the summer and winter seasons by modulation of precession (Hays et al., 1976; Imbrie et al., 1984; Paillard, 2021). Therefore, the eccentricity might have enhanced (reduced) the effect of obliquity during austral winter, regulating Antarctic sea ice (Yin, 2013). Similar spectral power between eccentricity and obliquity in both REDFIT

`

results from $\Delta\delta^{13}C_{w-e}$ and IRD records support our assumption of the combined effect of these two forcings on sea ice (Fig. 4C and D). Our analysis further suggests that the impact of obliquity on South Atlantic paleoceanography is intensified or weakened proportionally to the eccentricity value. Specifically, when eccentricity surpasses a threshold of 0.04 (or 0.02), the effects of obliquity on insolation are amplified (or reduced), which intensifies (reduces) winter insolation that reduces (enhances) sea ice extent (Supplementary Fig. 3). These findings are consistent with previous research by Lessa et al. (2019), who identified similar thresholds from surface water observations on core GL-854.

RAMPFIT phases II and IV occur when eccentricity values are above the threshold of 0.04, which boosts seasonal insolation, reducing the sea ice. On the other hand, RAMPFIT phases I and III occur when eccentricity reaches below the threshold of 0.02. It is important to consider the transience of the climate system associated with the accumulated energy over time, particularly in the Southern Hemisphere. Even though low $\Delta\delta^{13}C_{w-e}$ phases I and III comprise intervals in which eccentricity levels were above 0.02 (730-660 ka and 350-260 ka), they occurred after an interval with nearly two eccentricity cycles of values lower than 0.02 (800-730 ka and 460-350 ka). In this scenario, longer periods of low eccentricity values may have dumpened the effect of increasing eccentricity to values above 0.02 on insolation, which did not add enough energy to cause substantial changes in sea ice. Only when eccentricity crosses the threshold of 0.04, it enhances insolation adding enough energy to cause changes at high latitudes to promote phases II and IV. Eccentricity values below 0.02 also occur during the major decrease in $\Delta\delta^{13}C_{w-e}$ during MIS 4 when average $\Delta\delta^{13}C_{w-e}$ values are high through phase IV. From MIS 4 toward the Holocene, eccentricity values are below 0.02, hence we expect decreased insolation received at high latitudes through the added effect of amplified low obliquity forcing at MIS 4. This orbital configuration at MIS 4 could have promoted another change point on circulation to reduced AMOC toward the present day, although our record cannot confirm it.

`

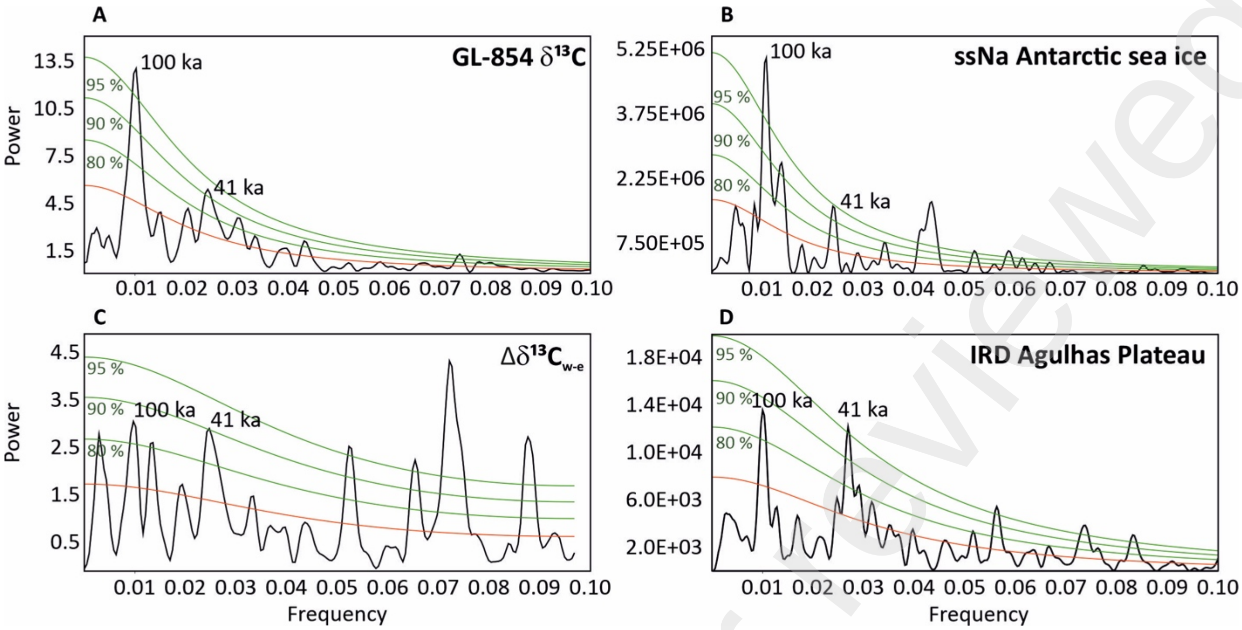

Figure 4 – REDFIT spectral analysis results performed in A) GL-854 $\delta^{13}C$, B) Dome C ssNa, C) $\Delta\delta^{13}C_{w\text{-}}e$, and D) Agulhas Plateau IRD records reveal relevant spectral power (Y axes) above the 90% confidence intervals in the obliquity and eccentricity frequency domains (X axes). Confidence level base lines (green and orange) and significant spectral periodicities are indicated.

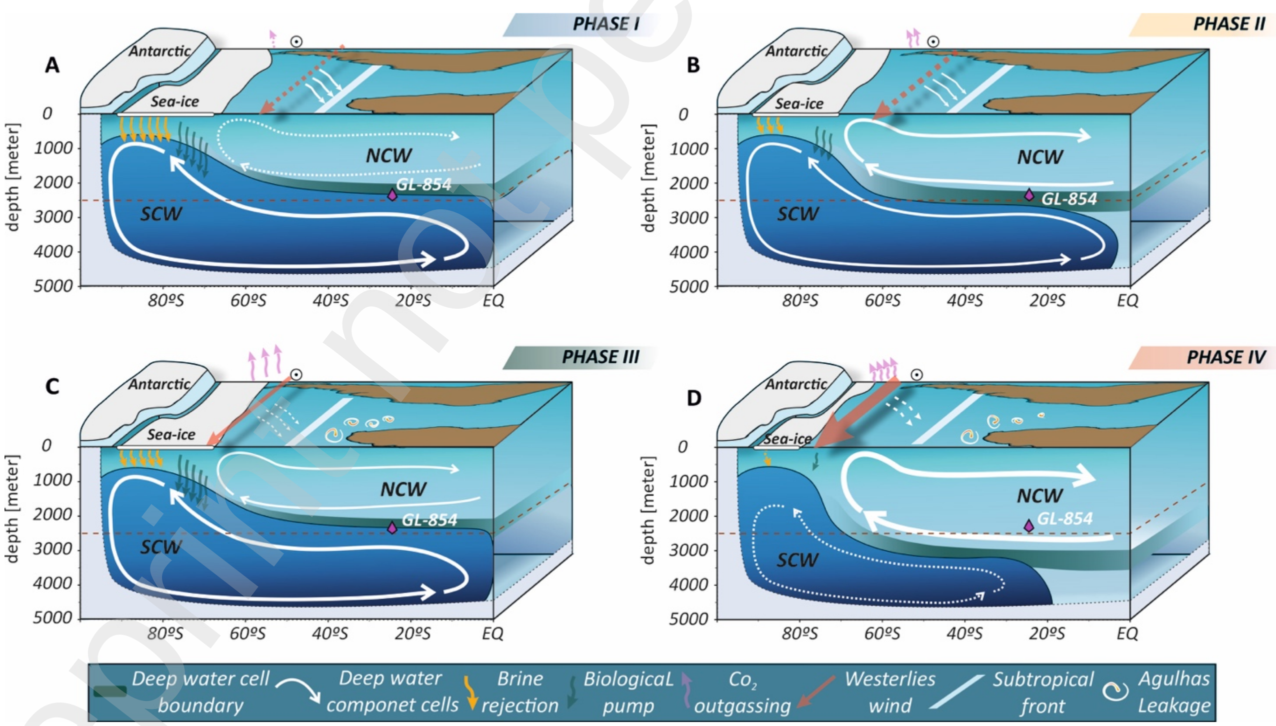

Figure 5 – Schematic representation of the main processes resultant of Antarctic sea ice extent variability through RAMPFIT phases A) I, B) II, C) III, and D) IV. *Phase*s II and IV show similar scenarios with reduced sea ice extent, decreased brine rejection, and hence reduced Antarctic Bottom Water (AABW) formation. Reduced sea ice extent also promotes the southward latitudinal displacement of the Westerlies and subtropical front, increasing Agulhas Leakage (AL) that

contributes to increasing North Atlantic Deep Water (NADW) production. Higher interglacial sea-ice melting and the AL reactivation after MIS 12 would explain the main difference between phases II and IV that led to more extended NADW southward penetration during phase IV. RAMPFIT phases I and III show increased glacial sea ice extent, enhanced brine rejection and increased Antarctic Bottom Water (AABW) formation. During these phases, very low AABW $\delta^{13}C$ values are due to the enhanced biological pump, and AABW penetrates further north, reaching up to 2200 m depth, reducing $\Delta\delta^{13}C_{w-e}$. The main difference between phases I and III is related to the AL intensification during phase III. In this phase, the AL effect on NADW during MIS 11 and MIS 9 may have been compensated by the intense glacial stages at MIS 12 and MIS 10. The vertical movements of the boundary between NADW and AABW are represented. Combined, these processes drive substantial changes in deep-water properties and formation, affecting Atlantic Meridional Overturning Circulation. Diagrams and symbols are described in the figure. Darker and lighter background colors represent denser and less dense deep-water cells, respectively of AABW and NADW.

5 Conclusions

Our study presents a new subtropical benthic foraminiferal $\delta^{13}C$ record from sediment core GL-854 collected from the Brazilian margin at mid-depth (2200 m), covering the last ca. 800 ka. Core GL-854 is ideally located for investigating past G-IG NADW variability in the South Atlantic basin. We compare this record to ODP Site 1264 $\delta^{13}C$ to calculate a zonal benthic foraminifera gradient ($\Delta\delta^{13}C_{w-e}$) record between DWBC and DEBC, providing insights into past NADW variability in the South Atlantic. Our zonal gradient increases (decreases) in response to the increased influence of NADW (AABW), recording variations between different AMOC states.

RAMPFIT trend estimations reveal an oscillatory behavior between weak and strong AMOC modes, highlighting the sensibility of our proxy to vertical movements of the boundary between NADW and AABW. The $\Delta\delta^{13}C_{w-e}$ increase after ca. 300 ka (phase IV) points to enhanced southward penetration of NADW that preferentially carries a modified signal through the DWBC towards the WSA instead of towards the eastern side of the basin. We attribute it to the AMOC intensification after the MBT, which does not exclusively respond to the NADW, but the enhanced contribution of low glacial AABW $\delta^{13}C$ to depths close to 2200 m between MIS 12 and MIS 8 likely also played a role. This suggests that both AMOC cells were more intense after the MBT. The contribution of AL reactivation after the MBT (our phase III) is possibly compensated by the strong glacial character of the $\Delta\delta^{13}C_{w-e}$ record, which prevented the expression of enhanced NADW production in our gradient during MIS 11 and MIS 9, and might have promoted the aforementioned later response after ca. 300 ka. Our $\Delta\delta^{13}C_{w-e}$ record mainly responds to the long-term patterns in the deep-water seesaw, revealing different AMOC states over the last ca. 800 ka, driven by variations in the AABW formation rate, ultimately affecting the NADW and the $\delta^{13}C$ distribution in the Atlantic (Buizert and Schmittner, 2015).

The major control behind the deep-water seesaw dynamic is ascribed to Antarctic sea-ice variability. During periods of lower (higher) sea ice, reduced (enhanced) brine rejection diminished (intensified) AABW formation, decreasing (increasing) deep stratification (Paillard and Parrenin, 2004; Bouttes et al., 2010). This has a direct impact on AABW and NADW mixing within the Atlantic, enhancing (reducing) the southward penetration of NADW that boosted (reduced) AMOC intensity and deepened (shallowed) the boundary between these deep-water cells. Therefore, expansion and contractions in sea ice allowed the establishment of four different AMOC phases due to its controls in the deep-water seesaw that changed Atlantic water mass geometry. We agree with the hypothesis that in the G-IG time scale, a vigorous AMOC state would demand reduced Southern Ocean sea ice (Ferrari et al., 2014; Nadeau et al., 2019).

Spectral analysis supports an orbital influence over the Antarctic sea ice propagated from high latitudes toward South Atlantic subtropical regions by exercising controls over the deep-water seesaw. The orbitally triggered mechanism is controlled by the combined effects of obliquity and eccentricity forcing the seasonal insolation, mainly regulating the build-up of sea ice during austral winter. Minimum (0.02) and maximum (0.04) threshold values of eccentricity are critical in amplifying or diminishing the obliquity effects at high latitudes. The synergic effect of the obliquity when eccentricity crosses these thresholds establishes specific insolation configurations that regulate the sea ice extent and promote the transitions between our RAMPFIT phases. Lower $\Delta\delta^{13}C_{w-e}$ phases I and III are established under low obliquity when eccentricity is maintained below the threshold of 0.02, while higher phases II and IV are established under high obliquity when eccentricity crosses values of 0.04. We argue that these phases refer to discrete states of the Late Pleistocene deep-water circulation and climate system (Schmieder et al., 2000; Barth et al., 2018), driven by the transitions among the various combinations of insolation conditions (Yin, 2013).

Near-200 ka cycles have been previously documented in paleoclimate records, usually ascribed to a 173-ka modulation of the obliquity cycle (Boulila et al., 2011; Westerhold et al., 2005; Huang et al., 2021) or interpreted either as a harmonic frequency of the 400-ka cycle or as a double 100-ka cycle (Hilgen et al., 2015). Considering the eccentricity variations over the last 800 ka, major transitions should occur nearly every two eccentricity cycles, i.e., related to long-term increasing trends from minimum to maximum eccentricity and vice versa. Although these low frequencies are relatively too weak to be identified by spectral analysis under untreated data, the periodicity of the RAMPFIT phases is close to a 200-ka-like cycle. It would agree with recent findings revealing a ~200 ka eccentricity cycle for the first time accounting for it as a component of the eccentricity forcing (Hilgen et al., 2020). Therefore, our orbital hypothesis and related periodic oscillations between different AMOC modes would be coherent with the 200-ka cycle eccentricity component despite the relation being speculative.

We have proposed a framework exploring the role of the deep-water seesaw in sustaining orbitally-triggered variations on Antarctic sea ice that significantly impact the oceanic carbon cycle. Our proposed mechanism connects the sea ice and ocean-atmosphere dynamics to deep-water geometry within the South Atlantic basin, which ultimately may have contributed to climate change across the MBT. Despite these AMOC modes and transitions probably having an orbital nature, the internal mechanisms in response to insolation forcing play a crucial role in propagating orbital effects on the climate (Barth et al., 2018; Caley et al., 2012; Yin, 2013). The explored South Atlantic controls on deep-water circulation might be responsible for an unclear MBT signal in North Atlantic climate records (Candy and McClymont, 2013). We further suggest that our RAMPFIT phases could possibly be related to the paleoceanographic changes throughout the shift from dominant 41-ka glacial-interglacial cycles to longer 100-ka cycles across the Mid-Pleistocene Transition (MPT; Hays et al., 1976; Pisias and Moore, 1981). Although longer records need to be used to establish a better relation with the MPT, our interpretations would also converge with interpretations showing major AMOC transitions occurring across this event (Schmieder et al., 2000; Pena and Goldstein, 2014; Kim et al., 2021). Furthermore, our findings are relevant for better understanding the internal climate responses and feedbacks in a significantly reduced sea ice expected in a global warming scenario.

`

Authorship contribution statement

Ballalai, J.M.: writing – original draft, conceptualization. Vazquez Riveiros, N.: review and editing, supervision. Santos, T.P.; Nascimento, R. A.; Piacsek, P.; Venancio, I.M.; Dias, B. B.; Belem, A.: writing – review and editing. Costa, K. B.; Toledo, F.: writing – review and editing, core donation. Mudelsee, M.: writing – review and statistical analysis. Albuquerque, A.L.S.: supervision, project administration, funding acquisition.

Acknowledgments

We thank Petrobras for providing the sediment core used in this study. This study was supported by the CAPES-ASpECTO project (grant 88887.091731/2014-01), CNPq-Aspecto (grant 429767/2018-8), CAPES-PRINT CLIMATE Project (grant 88887.528872/2020-00). R.A.N. acknowledges the CAPES grant 88887.176103/2018-00. P.P. acknowledges the CAPES-ASPECTO project grant 88887.091731/ 2014-01, and the postdoc fellowship of DGAPA-UNAM/2021. I.M.V. acknowledges UFF for FOPESQ 2022, CAPES grant 88881.512929/2020-01 and the Alexander von Humboldt Foundation. This study was also funded by FAPERJ (SEI-260003/000677/2023), which currently financially supports I.M.V. with a JCNE grant (200.120/2023 – 281226). B.B.D. acknowledges the financial support from FAPESP (grants 2022/01056-9, 2020/11452-3, and 2018/15123-4). This work was supported by the French National program LEFE (*Les Enveloppes fluids et l'Environnement*) and by ISblue (Interdisciplinary graduate school for the blue planet, ANR-17-EURE-0015) project and co-funded by a grant from the French government under the program "Investissements d'Avenir" embedded in France 2030. We thank the staff of the *Laboratório de Paleoceanografia do Atlantico Sul* (LaPAS-IO/USP) for sample preparation and the technicians and engineers from *Universitat Autonoma de Barcelona* for the isotopic analysis. The data reported in this paper is available in PANGAEA (www.pangaea.de).

References

Bard, E., Rickaby, R.E.M., 2009. Migration of the subtropical front as a modulator of glacial climate. Nature 460, 380–383. https://doi.org/10.1038/nature08189

Barth, A.M., Clark, P.U., Bill, N.S., He, F., Pisias, N.G., 2018. Climate evolution across the Mid-Brunhes Transition. Climate of the Past 14, 2071–2087. https://doi.org/10.5194/cp-14-2071-2018

Beal, L.M., De Ruijter, W.P.M., Biastoch, A., Zahn, R., Cronin, M., Hermes, J., Lutjeharms, J., Quartly, G., Tozuka, T., Baker-Yeboah, S., Bornman, T., Cipollini, P., Dijkstra, H., Hall, I., Park, W., Peeters, F., Penven, P., Ridderinkhof, H., Zinke, J., 2011. On the role of the Agulhas system in ocean circulation and climate. Nature 472, 429–436. https://doi.org/10.1038/nature09983

Beal, L.M., Elipot, S., 2016. Broadening not strengthening of the Agulhas Current since the early 1990s. Nature 540, 570–573. https://doi.org/10.1038/nature19853

Becquey, S., Gersonde, R., 2002. Past hydrographic and climatic changes in the Subantarctic Zone of the South Atlantic – The Pleistocene record from ODP Site 1090. Palaeogeogr Palaeoclimatol Palaeoecol 182, 221–239. https://doi.org/10.1016/S0031-0182(01)00497-7

Bell, D.B., Jung, S.J.A., Kroon, D., Lourens, L.J., Hodell, D.A., 2014. Local and regional trends in Plio-Pleistocene $\delta^{18}O$ records from benthic foraminifera. Geochemistry, Geophysics, Geosystems 15, 3304–3321. https://doi.org/10.1002/2014GC005297

Berger, W.H., Wefer, G., 2003. On the dynamics of the ice ages: Stage-11 Paradox, mid-brunhes climate shift, and 100-ky cycle, in: Geophysical Monograph Series. pp. 41–59. https://doi.org/10.1029/137GM04

Biastoch, A., Durgadoo, J. V., Morrison, A.K., van Sebille, E., Weijer, W., Griffies, S.M., 2015. Atlantic multi-decadal oscillation covaries with Agulhas leakage. Nat Commun 6, 10082. https://doi.org/10.1038/ncomms10082

Billups, K., Vizcaíno, M., Chiarello, J., Kaiser, E., 2020. Reconstructing western boundary current stability in the North Atlantic Ocean for the past 700 kyr from Globorotalia truncatulinoides coiling ratios. Paleoceanogr Paleoclimatol 0–3. https://doi.org/10.1029/2020PA003958

Blaauw, M., Christen, J.A., Bennett, K.D., Reimer, P.J., 2018. Double the dates and go for Bayes — Impacts of model choice, dating density and quality on chronologies. Quat Sci Rev 188, 58–66. https://doi.org/10.1016/j.quascirev.2018.03.032

Bordbar, M.H., Mohrholz, V., Schmidt, M., 2021. The relation of wind-driven coastal and offshore upwelling in the Benguela Upwelling System. J Phys Oceanogr 51, 3117–3133. https://doi.org/10.1175/JPO-D-20-0297.1

Boulila, S., Galbrun, B., Miller, K.G., Pekar, S.F., Browning, J. V., Laskar, J., Wright, J.D., 2011. On the origin of Cenozoic and Mesozoic “third-order” eustatic sequences. Earth Sci Rev 109, 94–112. https://doi.org/10.1016/j.earscirev.2011.09.003

Bouttes, N., Paillard, D., Roche, D.M., 2010. Impact of brine-induced stratification on the glacial carbon cycle. Climate of the Past 6, 575–589. https://doi.org/10.5194/cp-6-575-2010

Broecker, W.S., 1998. Paleocean circulation during the lst deglaciation: A bipolar seasaw? Paleoceanography 13, 119–121.

Broecker, W.S., Bond, G., Klas, M., Bonani, G., Wolfli, W., 1990. A salt oscillator in the glacial Atlantic? 1. The concept. Paleoceanography 5, 469–477. https://doi.org/10.1029/PA005i004p00469

Buizert, C., Schmittner, A., 2015. Southern Ocean control of glacial AMOC stability and Dansgaard-Oeschger interstadial duration. Paleoceanography 30, 1595–1612. https://doi.org/10.1002/2015PA002795

Caley, T., Giraudeau, J., Malaize, B., Rossignol, L., Pierre, C., 2012. Agulhas leakage as a key process in the modes of Quaternary climate changes. Proceedings of the National Academy of Sciences 109, 6835–6839. https://doi.org/10.1073/pnas.1115545109

Caley, T., Peeters, F.J.C., Biastoch, A., Rossignol, L., van Sebille, E., Durgadoo, J., Malaizé, B., Giraudeau, J., Arthur, K., Zahn, R., 2014. Quantitative estimate of the paleo-Agulhas leakage. Geophys Res Lett 41, 1238–1246. https://doi.org/10.1002/2014GL059278

Candy, I., McClymont, E.L., 2013. Interglacial intensity in the North Atlantic over the last 800 000 years: investigating the complexity of the mid-Brunhes Event. J Quat Sci 28, 343–348. https://doi.org/10.1002/jqs.2632

Curry, W.B., Oppo, D.W., 2005. Glacial water mass geometry and the distribution of $\delta^{13}C$ of ΣCO_2 in the western Atlantic Ocean. Paleoceanography 20, 1–12. https://doi.org/10.1029/2004PA001021

de Almeida, F.K., de Mello, R.M., Costa, K.B., Toledo, F.A.L., 2015. The response of deep-water benthic foraminiferal assemblages to changes in paleoproductivity during the Pleistocene (last 769.2 kyr), western South Atlantic Ocean. Palaeogeogr Palaeoclimatol Palaeoecol 440, 201–212. https://doi.org/10.1016/j.palaeo.2015.09.005

Diekmann, B., Kuhn, G., 2002. Sedimentary record of the mid-Pleistocene climate transition in the southeastern South Atlantic (ODP Site 1090). Palaeogeogr Palaeoclimatol Palaeoecol 182, 241–258. https://doi.org/10.1016/S0031-0182(01)00498-9

Droxler, A.W., Alley, R.B., Howard, W.R., Poore, R.Z., Burckle, L.H., 2003. Unique and exceptionally long interglacial marine isotope stage 11: Window into Earth warm future climate, in: Geophysical Monograph Series. pp. 1–14. https://doi.org/10.1029/137GM01

Duplessy, J.C., Shackleton, N.J., Fairbanks, R.G., Labeyrie, L., Oppo, D., Kallel, N., 1988. Deepwater source variations during the last climatic cycle and their impact on the global deepwater circulation. Paleoceanography 3, 343–360. https://doi.org/10.1029/PA003i003p00343

Eide, M., Olsen, A., Ninnemann, U.S., Johannessen, T., 2017. A global ocean climatology of preindustrial and modern ocean $\delta^{13}C$. Global Biogeochem Cycles 31, 515–534. https://doi.org/10.1002/2016GB005473

Ferrari, R., Jansen, M.F., Adkins, J.F., Burke, A., Stewart, A.L., Thompson, A.F., 2014. Antarctic sea ice control on ocean circulation in present and glacial climates. Proceedings of the National Academy of Sciences 111, 8753–8758. https://doi.org/10.1073/pnas.1323922111

Flower, B.P., Oppo, D.W., McManus, J.F., Venz, K.A., Hodell, D.A., Cullen, J.L., 2000. North Atlantic Intermediate to Deep Water circulation and chemical stratification during the past 1 Myr. Paleoceanography 15, 388–403. https://doi.org/10.1029/1999PA000430

Gordon, A.L., 1986. Interocean exchange of thermocline water. J Geophys Res 91, 5037. https://doi.org/10.1029/JC091iC04p05037

Hammer, O., Harper, D., Ryan, P., 2001. PAST: Paleontological Statistics Software Package for Education and Data Analysis. Palaeontologia Electronica 4, 1–9.

Hays, J.D., Imbrie, J., Shackleton, N.J., 1976. Variations in the Earth's Orbit: Pacemaker of the Ice Ages. Science (1979) 194, 1121–1132. https://doi.org/10.1126/science.194.4270.1121

Hilgen, F., Zeeden, C., Laskar, J., 2020. Paleoclimate records reveal elusive ~200-kyr eccentricity cycle for the first time. Glob Planet Change 194, 103296. https://doi.org/10.1016/j.gloplacha.2020.103296

Hilgen, F.J., Abels, H.A., Kuiper, K.F., Lourens, L.J., Wolthers, M., 2015. Towards a stable astronomical time scale for the Paleocene: Aligning Shatsky Rise with the Zumaia - Walvis Ridge ODP site 1262 composite. Newsl Stratigr 48, 91–110. https://doi.org/10.1127/nos/2014/0054

Hodell, D. a., Venz, K. a., Charles, C.D., Ninnemann, U.S., 2003. Pleistocene vertical carbon isotope and carbonate gradients in the South Atlantic sector of the Southern Ocean. Geochemistry, Geophysics, Geosystems 4, 1–19. https://doi.org/10.1029/2002GC000367

Hodell, D.A., 1993. Late Pleistocene Paleoceanography of the South Atlantic Sector of the Southern Ocean: Ocean Drilling Program Hole 704A. Paleoceanography 8, 47–67. https://doi.org/10.1029/92PA02774

Hodell, D.A., Channell, J.E.T., 2016. Mode transitions in Northern Hemisphere glaciation: co-evolution of millennial and orbital variability in Quaternary climate. Climate of the Past 12, 1805–1828. https://doi.org/10.5194/cp-12-1805-2016

Holden, P.B., Edwards, N.R., Wolff, E.W., Valdes, P.J., Singarayer, J.S., 2011. The Mid-Brunhes Event and West Antarctic ice sheet stability. J Quat Sci 26, 474–477. https://doi.org/10.1002/jqs.1525

Huang, H., Gao, Y., Ma, C., Jones, M.M., Zeeden, C., Ibarra, D.E., Wu, H., Wang, C., 2021. Organic carbon burial is paced by a ~173-ka obliquity cycle in the middle to high latitudes. Sci Adv 7, 1–11. https://doi.org/10.1126/sciadv.abf9489

Imbrie, J., Berger, A., Boyle, E.A., Clemens, S.C., Duffy, A., Howard, W.R., Kukla, G., Kutzbach, J., Martinson, D.G., McIntyre, A., Mix, A.C., Molfino, B., Morley, J.J., Peterson, L.C., Pisias, N.G., Prell, W.L., Raymo, M.E., Shackleton, N.J., Toggweiler, J.R., 1993. On the structure and origin of major glaciation cycles 2. The 100,000-year cycle. Paleoceanography 8, 699–735. https://doi.org/10.1029/93PA02751

Imbrie, J., Hays, J.D., Martinson, D.G., McIntyre, A., Mix, A.C., Morley, J.J., Pisias, N.G., Prell and, W.L., Shackleton, N.J., 1984. The orbital theory of pleistocene climate: support from a revised chronology of the marine O180 record. In "Milankovitch and climate." Milankovitch and Climate 269–305.

Jansen, J.H.F., Kuijpers, A., Troelstra, S.R., 1986. A Mid-Brunhes Climatic Event: Long-Term Changes in Global Atmosphere and Ocean Circulation. Science (1979) 232, 619–622. https://doi.org/10.1126/science.232.4750.619

Jansen, M.F., 2017. Glacial ocean circulation and stratification explained by reduced atmospheric temperature. Proceedings of the National Academy of Sciences 114, 45–50. https://doi.org/10.1073/pnas.1610438113

Jansen, M.F., Nadeau, L.-P., 2016. The Effect of Southern Ocean Surface Buoyancy Loss on the Deep-Ocean Circulation and Stratification. J Phys Oceanogr 46, 3455–3470. https://doi.org/10.1175/JPO-D-16-0084.1

Jouzel, J., Masson-Delmotte, V., Cattani, O., Dreyfus, G., Falourd, S., Hoffmann, G., Minster, B., Nouet, J., Barnola, J.M., Chappellaz, J., Fischer, H., Gallet, J.C., Johnsen, S., Leuenberger, M., Loulergue, L., Luethi, D., Oerter, H., Parrenin, F., Raisbeck, G., Raynaud, D., Schilt, A., Schwander, J., Selmo, E., Souchez, R., Spahni, R., Stauffer, B., Steffensen, J.P., Stenni, B., Stocker, T.F., Tison, J.L., Werner, M., Wolff, E.W., 2007. Orbital and Millennial Antarctic Climate Variability over the Past 800,000 Years. Science (1979) 317, 793–796. https://doi.org/10.1126/science.1141038

Kemp, A.E.S., Grigorov, I., Pearce, R.B., Naveira Garabato, A.C., 2010. Migration of the Antarctic Polar Front through the mid-Pleistocene transition: evidence and climatic implications. Quat Sci Rev 29, 1993–2009. https://doi.org/10.1016/j.quascirev.2010.04.027

Kim, J., Goldstein, S.L., Pena, L.D., Jaume-Seguí, M., Knudson, K.P., Yehudai, M., Bolge, L., 2021. North Atlantic Deep Water during Pleistocene interglacials and glacials. Quat Sci Rev 269, 107146. https://doi.org/10.1016/j.quascirev.2021.107146

Kroopnick, P.M., 1985. The distribution of ^{13}C of ΣCO_2 in the world oceans. Deep Sea Research Part A. Oceanographic Research Papers 32, 57–84. https://doi.org/10.1016/0198-0149(85)90017-2

Lacourse, T., Gajewski, K., 2020. Current practices in building and reporting age-depth models. Quat Res 96, 28–38. https://doi.org/10.1017/qua.2020.47

Laskar, J., Robutel, P., Joutel, F., Gastineau, M., Correia, A.C.M., Levrard, B., 2004. A long-term numerical solution for the insolation quantities of the Earth. Astron Astrophys 428, 261–285. https://doi.org/10.1051/0004-6361:20041335

Lea, D.W., 1995. A trace metal perspective on the evolution of Antarctic Circumpolar Deep Water chemistry. Paleoceanography 10, 733–747. https://doi.org/10.1029/95PA01546

Lessa, D.V.O., Santos, T.P., Venancio, I.M., Santarosa, A.C.A., dos Santos Junior, E.C., Toledo, F.A.L., Costa, K.B., Albuquerque, A.L.S., 2019. Eccentricity-induced expansions of Brazilian coastal upwelling zones. Glob Planet Change 179, 33–42. https://doi.org/10.1016/j.gloplacha.2019.05.002

Lisiecki, L.E., Raymo, M.E., 2005. A Pliocene-Pleistocene stack of 57 globally distributed benthic $\delta^{18}O$ records. Paleoceanography 20. https://doi.org/https://doi.org/10.1029/2004PA001071

Lund, D.C., Tessin, A.C., Hoffman, J.L., Schmittner, A., 2015. Southwest Atlantic water mass evolution during the last deglaciation. Paleoceanography 30, 477–494. https://doi.org/10.1002/2014PA002657

Lüthi, D., Le Floch, M., Bereiter, B., Blunier, T., Barnola, J.-M., Siegenthaler, U., Raynaud, D., Jouzel, J., Fischer, H., Kawamura, K., Stocker, T.F., 2008. High-resolution carbon dioxide concentration record 650,000–800,000 years before present. Nature 453, 379–382. https://doi.org/10.1038/nature06949

Lynch-Stieglitz, J., Adkins, J.F., Curry, W.B., Dokken, T., Hall, I.R., Herguera, J.C., Hirschi, J.J.-M., Ivanova, E. V., Kissel, C., Marchal, O., Marchitto, T.M., McCave, I.N., McManus, J.F., Mulitza, S., Ninnemann, U., Peeters, F., Yu, E.-F., Zahn, R., 2007. Atlantic Meridional Overturning Circulation During the Last Glacial Maximum. Science (1979) 316, 66–69. https://doi.org/10.1126/science.1137127

Mackensen, A., Fu¨tterer, D.K., Grobe, H., Schmiedl, G., 1993. Benthic foraminiferal assemblages from the eastern South Atlantic Polar Front region between 35° and 57°S: Distribution, ecology and fossilization potential. Mar Micropaleontol 22, 33–69. https://doi.org/10.1016/0377-8398(93)90003-G

Marchitto, T.M., Broecker, W.S., 2006. Deep water mass geometry in the glacial Atlantic Ocean: A review of constraints from the paleonutrient proxy Cd/Ca. Geochemistry, Geophysics, Geosystems 7. https://doi.org/10.1029/2006GC001323

Marshall, J., Speer, K., 2012. Closure of the meridional overturning circulation through Southern Ocean upwelling. Nat Geosci 5, 171–180. https://doi.org/10.1038/ngeo1391

Martin, J.H., 1990. Glacial-interglacial CO_2 change: The Iron Hypothesis. Paleoceanography 5, 1–13. https://doi.org/10.1029/PA005i001p00001

Martínez-Garcia, A., Rosell-Melé, A., Geibert, W., Gersonde, R., Masqué, P., Gaspari, V., Barbante, C., 2009. Links between iron supply, marine productivity, sea surface temperature, and CO_2 over the last 1.1 Ma. Paleoceanography 24. https://doi.org/10.1029/2008PA001657

Martínez-Garcia, A., Rosell-Melé, A., Jaccard, S.L., Geibert, W., Sigman, D.M., Haug, G.H., 2011. Southern Ocean dust–climate coupling over the past four million years. Nature 476, 312–315. https://doi.org/10.1038/nature10310

Marzocchi, A., Jansen, M.F., 2019. Global cooling linked to increased glacial carbon storage via changes in Antarctic sea ice. Nat Geosci 12, 1001–1005. https://doi.org/10.1038/s41561-019-0466-8

Mitsui, T., Boers, N., 2022. Machine learning approach reveals strong link between obliquity amplitude increase and the Mid-Brunhes transition. Quat Sci Rev 277, 107344. https://doi.org/10.1016/j.quascirev.2021.107344

Mudelsee, M., 2014. Climate Time Series Analysis, Atmospheric and Oceanographic Sciences Library. Springer International Publishing, Cham. https://doi.org/10.1007/978-3-319-04450-7

Mudelsee, M., 2000. Ramp function regression: a tool for quantifying climate transitions. Comput Geosci 26, 293–307. https://doi.org/10.1016/S0098-3004(99)00141-7

Mudelsee, M., Schulz, M., 1997. The Mid-Pleistocene climate transition: onset of 100 ka cycle lags ice volume build-up by 280 ka. Earth Planet Sci Lett 151, 117–123. https://doi.org/10.1016/S0012-821X(97)00114-3

Muglia, J., Schmittner, A., 2021. Carbon isotope constraints on glacial Atlantic meridional overturning: Strength vs depth. Quat Sci Rev 257, 106844. https://doi.org/10.1016/j.quascirev.2021.106844

Nadeau, L.-P., Ferrari, R., Jansen, M.F., 2019. Antarctic Sea Ice Control on the Depth of North Atlantic Deep Water. J Clim 32, 2537–2551. https://doi.org/10.1175/JCLI-D-18-0519.1

Oppo, D.W., Horowitz, M., 2000. Glacial deep water geometry: South Atlantic benthic foraminiferal Cd/Ca and $\delta^{13}C$ evidence. Paleoceanography 15, 147–160. https://doi.org/10.1029/1999PA000436

Paillard, D., 2021. Climate and Astronomical Cycles, in: Ramstein Gilles and Landais, A. and B.N. and S.P. and G.A. (Ed.), Paleoclimatology. Springer International Publishing, Cham, pp. 385–404. https://doi.org/10.1007/978-3-030-24982-3_28

Paillard, D., Labeyrie, L., Yiou, P., 1996. Macintosh Program performs time-series analysis. Eos, Transactions American Geophysical Union 77, 379. https://doi.org/https://doi.org/10.1029/96EO00259

Paillard, D., Parrenin, F., 2004. The Antarctic ice sheet and the triggering of deglaciations. Earth Planet Sci Lett 227, 263–271. https://doi.org/10.1016/j.epsl.2004.08.023

Peeters, F.J.C., Acheson, R., Brummer, G.-J.A., de Ruijter, W.P.M., Schneider, R.R., Ganssen, G.M., Ufkes, E., Kroon, D., 2004. Vigorous exchange between the Indian and Atlantic oceans at the end of the past five glacial periods. Nature 430, 661–665. https://doi.org/10.1038/nature02785

Pena, L.D., Goldstein, S.L., 2014. Thermohaline circulation crisis and impacts during the mid-Pleistocene transition. Science (1979) 345, 318–322. https://doi.org/10.1126/science.1249770

Peterson, C.D., Lisiecki, L.E., 2018. Deglacial carbon cycle changes observed in a compilation of 127 benthic $\delta^{13}C$ time series (20–6 ka). Climate of the Past 14, 1229–1252. https://doi.org/10.5194/cp-14-1229-2018

Petit, J.R., Delmonte, B., 2009. A model for large glacial–interglacial climate-induced changes in dust and sea salt concentrations in deep ice cores (central Antarctica): palaeoclimatic implications and prospects for refining ice core chronologies. Tellus B: Chemical and Physical Meteorology 61, 768. https://doi.org/10.1111/j.1600-0889.2009.00437.x

`

Petit, J.R., Jouzel, J., Raynaud, D., Barkov, N.I., Barnola, J.-M., Basile, I., Bender, M., Chappellaz, J., Davis, M., Delaygue, G., Delmotte, M., Kotlyakov, V.M., Legrand, M., Lipenkov, V.Y., Lorius, C., PÉpin, L., Ritz, C., Saltzman, E., Stievenard, M., 1999. Climate and atmospheric history of the past 420,000 years from the Vostok ice core, Antarctica. Nature 399, 429–436. https://doi.org/10.1038/20859

Piola, A.R., Matano, R.P., 2019. Ocean Currents: Atlantic Western Boundary—Brazil Current/Falkland (Malvinas) Current, in: Encyclopedia of Ocean Sciences. Elsevier, pp. 414–420. https://doi.org/10.1016/B978-0-12-409548-9.10541-X

Pisias, N.G., Moore, T.C., 1981. The evolution of Pleistocene climate: A time series approach. Earth Planet Sci Lett 52, 450–458. https://doi.org/10.1016/0012-821X(81)90197-7

Rahmstorf, S., 2006. Thermohaline Ocean Circulation, in: Encyclopedia of Quaternary Science.

Raymo, M.E., Oppo, D.W., Curry, W., 1997. The Mid-Pleistocene climate transition: A deep sea carbon isotopic perspective. Paleoceanography 12, 546–559. https://doi.org/10.1029/97PA01019

Razik, S., Govin, A., Chiessi, C.M., von Dobeneck, T., 2015. Depositional provinces, dispersal, and origin of terrigenous sediments along the SE South American continental margin. Mar Geol 363, 261–272. https://doi.org/10.1016/j.margeo.2015.03.001

Röthlisberger, R., Crosta, X., Abram, N.J., Armand, L., Wolff, E.W., 2010. Potential and limitations of marine and ice core sea ice proxies: an example from the Indian Ocean sector. Quat Sci Rev 29, 296–302. https://doi.org/10.1016/j.quascirev.2009.10.005

Röthlisberger, R., Mudelsee, M., Bigler, M., de Angelis, M., Fischer, H., Hansson, M., Lambert, F., Masson-Delmotte, V., Sime, L., Udisti, R., Wolff, E.W., 2008. The Southern Hemisphere at glacial terminations: insights from the Dome C ice core. Climate of the Past 4, 345–356. https://doi.org/10.5194/cp-4-345-2008

Sarntheim, M., Erlenkeuser, H., Grafenstein, R. von, Schröder, C., 1984. Stable-isotope stratigraphy for the last 750,000 years : “Meteor” core 13519 from the eastern equatorial Atlantic. Meteor Forschungsergebnisse: Reihe C, Geologie und Geophysik 38, 9–24.

Sarnthein, M., Tiedemann, R., 1989. Toward a High-Resolution Stable Isotope Stratigraphy of the Last 3.4 Million Years: Sites 658 and 659 off Northwest Africa, in: Proceedings of the Ocean Drilling Program, 108 Scientific Results. Ocean Drilling Program, pp. 167–185. https://doi.org/10.2973/odp.proc.sr.108.159.1989

Schmieder, F., von Dobeneck, T., Bleil, U., 2000. The Mid-Pleistocene climate transition as documented in the deep South Atlantic Ocean: initiation, interim state and terminal event. Earth Planet Sci Lett 179, 539–549. https://doi.org/10.1016/S0012-821X(00)00143-6

Schmiedl, G., Mackensen, A., 1997. Late Quaternary paleoproductivity and deep water circulation in the eastern South Atlantic Ocean: Evidence from benthic foraminifera. Palaeogeogr Palaeoclimatol Palaeoecol 130, 43–80. https://doi.org/10.1016/S0031-0182(96)00137-X

`

Schmittner, A., Lund, D.C., 2015. Early deglacial Atlantic overturning decline and its role in atmospheric CO_2 rise inferred from carbon isotopes ($\delta^{13}C$). Climate of the Past 11, 135–152. https://doi.org/10.5194/cp-11-135-2015

Schulz, M., Mudelsee, M., 2002. REDFIT: estimating red-noise spectra directly from unevenly spaced paleoclimatic time series. Comput Geosci 28, 421–426. https://doi.org/10.1016/S0098-3004(01)00044-9

Siegenthaler, U., Stocker, T.F., Monnin, E., Lüthi, D., Schwander, J., Stauffer, B., Raynaud, D., Barnola, J.-M., Fischer, H., Masson-Delmotte, V., Jouzel, J., 2005. Stable Carbon Cycle - Climate Relationship During the Late Pleistocene. Science (1979) 310, 1313–1317. https://doi.org/10.1126/science.1120130

Siegfried, L., Schmidt, M., Mohrholz, V., Pogrzeba, H., Nardini, P., Böttinger, M., Scheuermann, G., 2019. The tropical-subtropical coupling in the Southeast Atlantic from the perspective of the northern Benguela upwelling system. PLoS One 14, e0210083. https://doi.org/10.1371/journal.pone.0210083

Sigman, D.M., Boyle, E.A., 2000. Glacial/interglacial variations in atmospheric carbon dioxide. Nature. https://doi.org/10.1038/35038000

Sigman, D.M., Hain, M.P., Haug, G.H., 2010. The polar ocean and glacial cycles in atmospheric CO_2 concentration. Nature 466, 47–55. https://doi.org/10.1038/nature09149

Skinner, L.C., Fallon, S., Waelbroeck, C., Michel, E., Barker, S., 2010. Ventilation of the Deep Southern Ocean and Deglacial CO_2 Rise. Science (1979) 328, 1147–1151. https://doi.org/10.1126/science.1183627

Starr, A., Hall, I.R., Barker, S., Rackow, T., Zhang, X., Hemming, S.R., van der Lubbe, H.J.L., Knorr, G., Berke, M.A., Bigg, G.R., Cartagena-Sierra, A., Jiménez-Espejo, F.J., Gong, X., Gruetzner, J., Lathika, N., LeVay, L.J., Robinson, R.S., Ziegler, M., 2021. Antarctic icebergs reorganize ocean circulation during Pleistocene glacials. Nature 589, 236–241. https://doi.org/10.1038/s41586-020-03094-7

Stephens, B.B., Keeling, R.F., 2000. The influence of Antarctic sea ice on glacial–interglacial CO_2 variations. Nature 404, 171–174. https://doi.org/10.1038/35004556

Stramma, L., England, M., 1999. On the water masses and mean circulation of the South Atlantic Ocean. J Geophys Res Oceans 104, 20863–20883. https://doi.org/10.1029/1999JC900139

Talley, L., 2013. Closure of the Global Overturning Circulation Through the Indian, Pacific, and Southern Oceans: Schematics and Transports. Oceanography 26, 80–97. https://doi.org/10.5670/oceanog.2013.07

Toggweiler, J.R., 1999. Variation of atmospheric CO_2 by ventilation of the ocean's deepest water. Paleoceanography 14, 571–588. https://doi.org/10.1029/1999PA900033

Toggweiler, J.R., Russell, J.L., Carson, S.R., 2006. Midlatitude westerlies, atmospheric CO_2, and climate change during the ice ages. Paleoceanography 21. https://doi.org/10.1029/2005PA001154

Vázquez Riveiros, N., Waelbroeck, C., Skinner, L., Duplessy, J.-C., McManus, J.F., Kandiano, E.S., Bauch, H.A., 2013. The “MIS 11 paradox” and ocean circulation: Role of millennial scale events. Earth Planet Sci Lett 371–372, 258–268. https://doi.org/10.1016/j.epsl.2013.03.036

Voigt, I., Cruz, A.P.S., Mulitza, S., Chiessi, C.M., Mackensen, A., Lippold, J., Antz, B., Zabel, M., Zhang, Y., Barbosa, C.F., Tisserand, A.A., 2017. Variability in mid-depth ventilation of the western Atlantic Ocean during the last deglaciation. Paleoceanography 32, 948–965. https://doi.org/10.1002/2017PA003095

Weijer, W., De Ruijter, W.P.M., Sterl, A., Drijfhout, S.S., 2002. Response of the Atlantic overturning circulation to South Atlantic sources of buoyancy. Glob Planet Change 34, 293–311. https://doi.org/10.1016/S0921-8181(02)00121-2

Westerhold, T., Bickert, T., Röhl, U., 2005. Middle to late Miocene oxygen isotope stratigraphy of ODP site 1085 (SE Atlantic): New constrains on Miocene climate variability and sea-level fluctuations. Palaeogeogr Palaeoclimatol Palaeoecol 217, 205–222. https://doi.org/10.1016/j.palaeo.2004.12.001

Wolff, E.W., Fischer, H., Fundel, F., Ruth, U., Twarloh, B., Littot, G.C., Mulvaney, R., Röthlisberger, R., de Angelis, M., Boutron, C.F., Hansson, M., Jonsell, U., Hutterli, M.A., Lambert, F., Kaufmann, P., Stauffer, B., Stocker, T.F., Steffensen, J.P., Bigler, M., Siggaard-Andersen, M.L., Udisti, R., Becagli, S., Castellano, E., Severi, M., Wagenbach, D., Barbante, C., Gabrielli, P., Gaspari, V., 2006. Southern Ocean sea-ice extent, productivity and iron flux over the past eight glacial cycles. Nature 440, 491–496. https://doi.org/10.1038/nature04614

Wolff, E.W., Rankin, A.M., Röthlisberger, R., 2003. An ice core indicator of Antarctic sea ice production? Geophys Res Lett 30. https://doi.org/10.1029/2003GL018454

Wu, Z., Yin, Q., Guo, Z., Berger, A., 2020. Hemisphere differences in response of sea surface temperature and sea ice to precession and obliquity. Glob Planet Change 192. https://doi.org/10.1016/j.gloplacha.2020.103223

Yin, Q., 2013. Insolation-induced mid-Brunhes transition in Southern Ocean ventilation and deep-ocean temperature. Nature 494, 222–225. https://doi.org/10.1038/nature11790

Yin, Q.Z., Berger, A., 2012. Individual contribution of insolation and CO_2 to the interglacial climates of the past 800,000 years. Clim Dyn 38, 709–724. https://doi.org/10.1007/s00382-011-1013-5

Yin, Q.Z., Berger, A., 2010. Insolation and CO_2 contribution to the interglacial climate before and after the Mid-Brunhes Event. Nat Geosci 3, 243–246. https://doi.org/10.1038/ngeo771

Yu, J., Menviel, L., Jin, Z.D., Thornalley, D.J.R., Barker, S., Marino, G., Rohling, E.J., Cai, Y., Zhang, F., Wang, X., Dai, Y., Chen, P., Broecker, W.S., 2016. Sequestration of carbon in the deep Atlantic during the last glaciation. Nat Geosci 9, 319–324. https://doi.org/10.1038/ngeo2657

Zachos, J.C., Kroon, D., Blum, P., et al., 2004. Proceedings of the Ocean Drilling Program, 208 Initial Reports, Proceedings of the Ocean Drilling Program, Initial Reports, Proceedings of the Ocean Drilling Program. Ocean Drilling Program. https://doi.org/10.2973/odp.proc.ir.208.2004

`

Atlantic $\delta^{13}C$ Deep-water Seesaw Controlled by Antarctic Sea Ice Over the Last 800 ka

João M. Ballalai[1, 2]*, Natalia Vázquez Riveiros[2], Thiago P. Santos[3], Rodrigo A. Nascimento[3], Manfred Mudelsee[4,5,6], Patrícia Piacsek[7], Igor M. Venancio[1], Bruna B. Dias[8], André Belem[9], Karen B. Costa[10], Felipe Toledo[10], Ana Luiza S. Albuquerque[3]

[1] Geochemistry Department, Fluminense Federal University, Niterói, Brazil

[2] UMR 6538 Geo-Ocean, CNRS, IFREMER, UBO, UBS, Plouzané, France

[3] Programa de Pós-Graduação Dinâmica dos Oceanos e da Terra (DOT-UFF), Fluminense Federal University

[4] University of Potsdam, Institute of Geosciences, Potsdam, Germany

[5] Climate Risk Analysis, Kreuzstrasse 27, Heckenbeck, 37581Bad Gandersheim, Germany

[6] Alfred Wegener Institute, Helmholtz Centre for Polar and Marine Research, Bussestrasse 24, 27570 Bremerhaven, Germany

[7] Centro de Geociencias, Universidad Nacional Autónoma de México (UNAM), Campus UNAM Juriquilla, Querértaro, Qro, Mexico, 76230

[8] School of Arts, Sciences and Humanities, University of São Paulo, São Paulo, Brazil

[9] Oceanographic Observatory, Fluminense Federal University, Niterói, Brazil

[10] South Atlantic Paleoceanography Laboratory, Oceanographic Institute, University of Sao Paulo, Sao Paulo, Brazil

Corresponding author: João M. Ballalai (joaoballalai@id.uff.br)

Full postal address: Chemistry Institute – Geochemistry Department, 5th floor. Outeiro São João Baptista s/n - Centro - Niterói, RJ - Brazil

This supporting information contains supplementary figures and tables of the main text.

Age model

In the main text we provided all main information regarding the original age model construction for GL-854 core published by de Almeida et al. (2015). Chosen tie points and calendar age vs. depth from the visual alignment with benthic foraminifera $\delta^{18}O$ global stack

LR04 (Lisiecki and Raymo, 2005) are indicated in the Supplementary Fig. 1 and 2 (de Almeida et al., 2015).

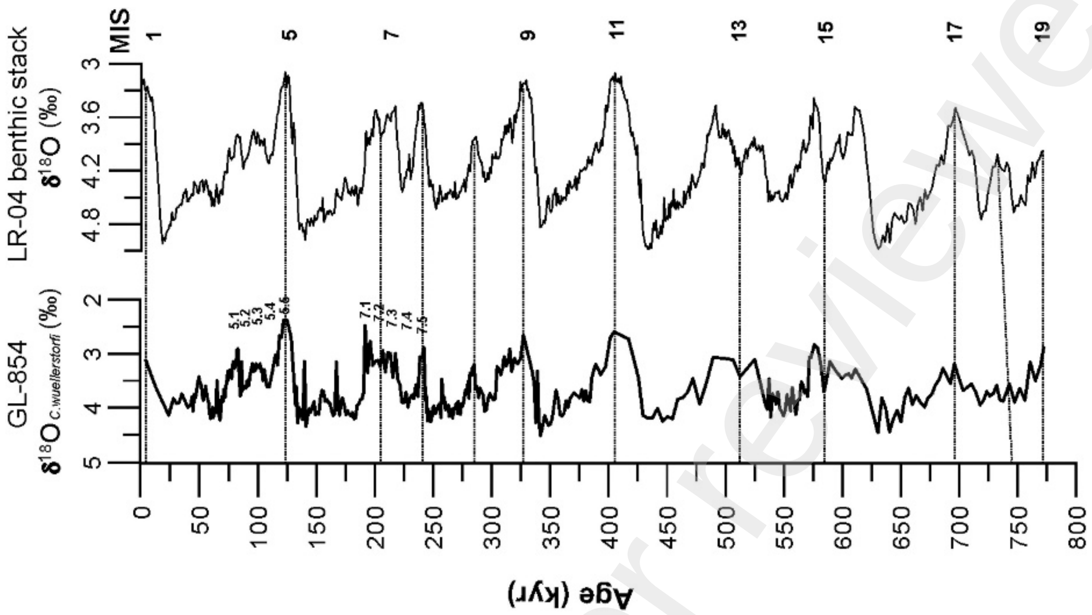

Figure 1 –Main tie points between core GL-854 and LR04 benthic stack (Lisiecki and Raymo, 2005; de Almeida et al., 2015).

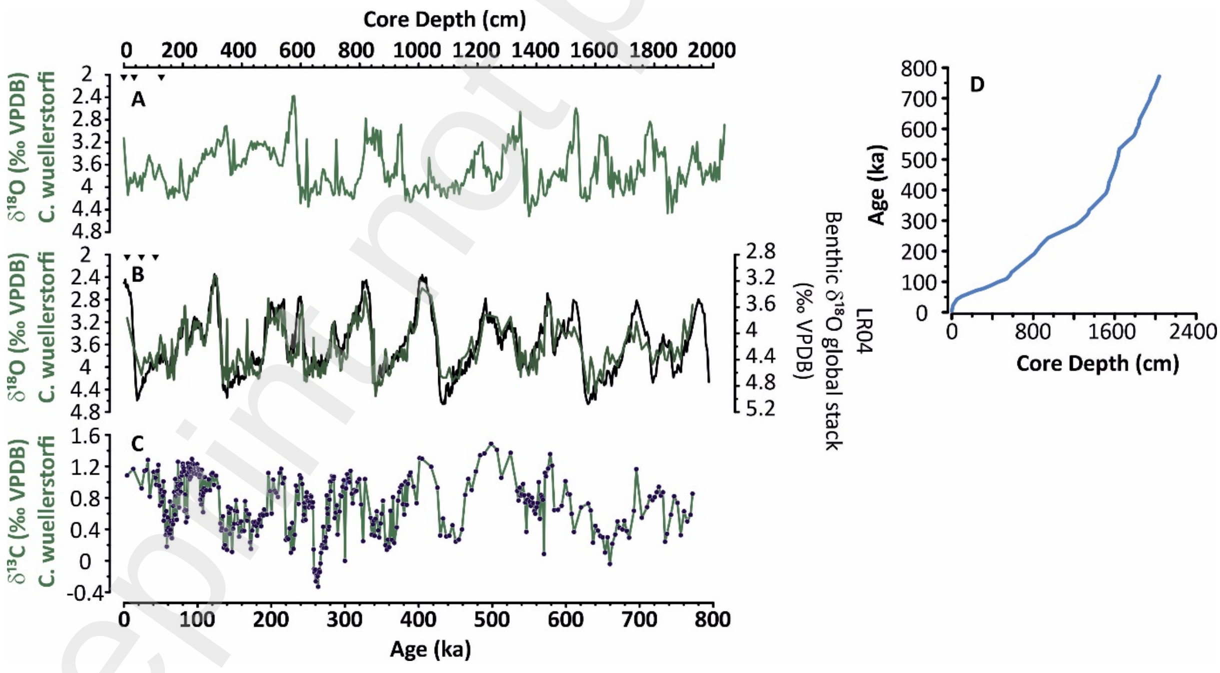

Figure 2 - Reference curve and age-depth model of core GL-854. Benthic foraminifera (*Cibicidoides wuellerstorfi*) A) $\delta^{18}O$ versus depth, B) $\delta^{18}O$ and LR04 benthic foraminifera $\delta^{18}O$ stack LR04 (Lisiecki and Raymo, 2005), C) $\delta^{13}C$ versus age, and D) age-depth model from de Almeida et al. (2015). Triangles represent the calibrated ^{14}C ages.

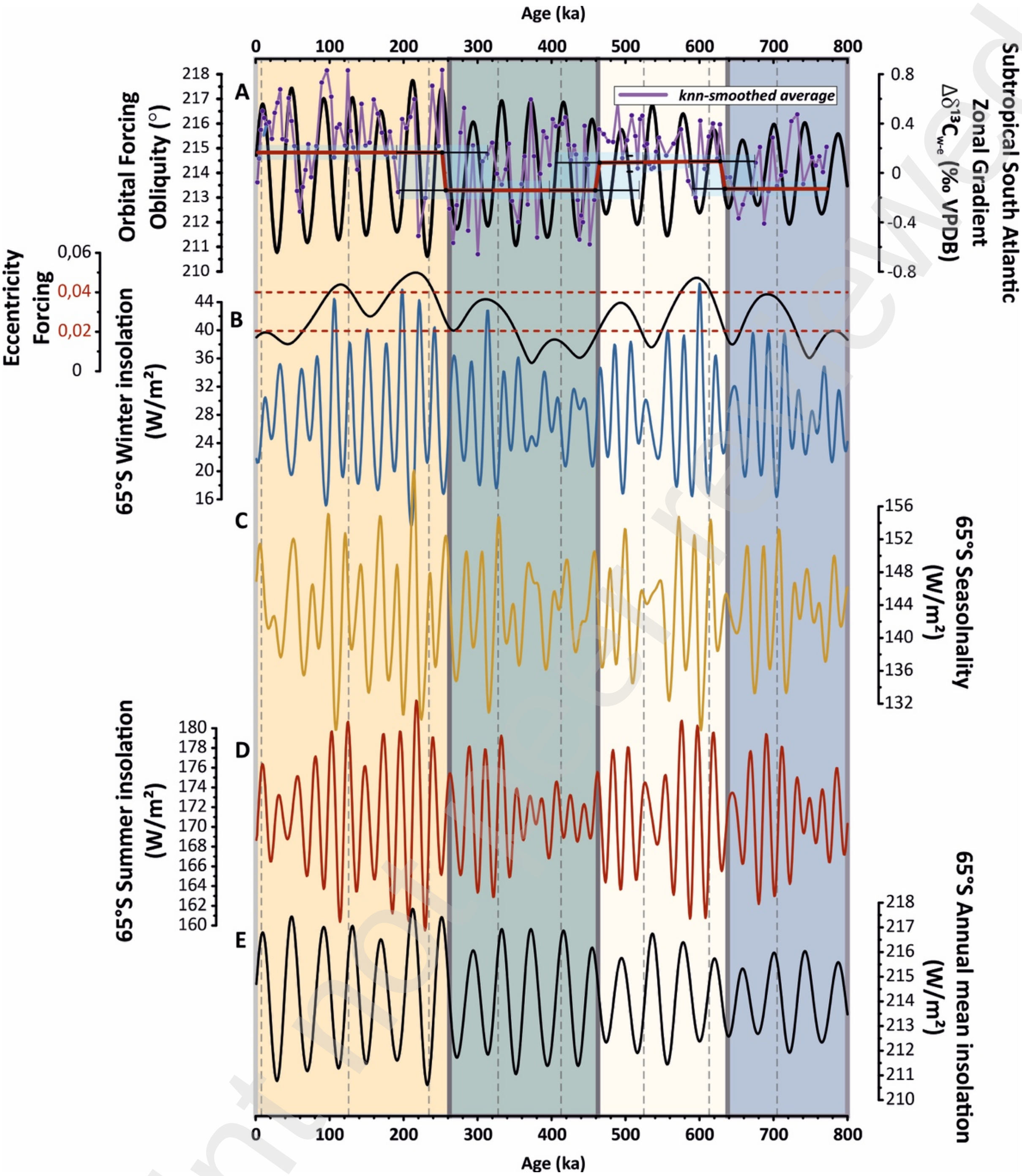

Figure 3: Orbital influence over 65°S insolation across RAMPFIT phases I, II, III, IV. a) $\Delta\delta^{13}C_{w-e}$ record and obliquity forcing; b) winter; c) seasonality; d) summer, and e) annual mean insolation, which varies in function of a) obliquity (Laskar et al., 2004).

References

de Almeida, F.K., de Mello, R.M., Costa, K.B., Toledo, F.A.L., 2015. The response of deep-water benthic foraminiferal assemblages to changes in paleoproductivity during the Pleistocene (last

769.2 kyr), western South Atlantic Ocean. Palaeogeogr Palaeoclimatol Palaeoecol 440, 201–212. https://doi.org/10.1016/j.palaeo.2015.09.005

Laskar, J., Robutel, P., Joutel, F., Gastineau, M., Correia, A.C.M., Levrard, B., 2004. A long-term numerical solution for the insolation quantities of the Earth. Astron Astrophys 428, 261–285. https://doi.org/10.1051/0004-6361:20041335

Lisiecki, L.E., Raymo, M.E., 2005. A Pliocene-Pleistocene stack of 57 globally distributed benthic δ 18O records. Paleoceanography 20, 1–17. https://doi.org/10.1029/2004PA001071